A Temperature- and Pressure-Sensitive Visco-Plasticity Theory based on Interface Mechanisms for Sedimentary Rocks

Mustafa Sari[1,2,*], Sotiris Alevizos[2], Thomas Poulet[1,2], Jack Lin[2], Manolis Veveakis[3]

Abstract

In this work, a multi-physics constitutive theory for sedimentary rocks is proposed combining the results of laboratory tests, theoretical analysis and numerical validation. The viscosity of the material is assumed to be a function of the temperature, pore-pressure and energy required to alter the intergranular interfaces. The latter is expressed through the chemical potentials of the phases involved during processes like chemical dissolution/precipitation of the interfaces or mechanical debonding.

The resulting flow law and corresponding stress equilibrium are coupled to the energy and mass conservation laws, constituting a closed system of equations. To solve this system, the theoretical framework is implemented using the Finite Element REDBACK simulator and its qualitative behaviour is analysed in monotonous and cyclic isotropic compression, as well as in direct shear for different loading rates. A series of numerical calibration tests

*m.sari@student.unsw.edu.au

[1]CSIRO Mineral Resources, 26 Dick Perry Avenue, Kensington, WA 6151, Australia

[2]School of Minerals and Energy Resources Engineering, UNSW, Kensington, NSW 2033, Australia

[3]Civil and Environmental Engineering, Duke University, Durham NC, USA

is then successfully performed against different types of rocks (sandstone, mudstone), saturating conditions (dry, wet), stress paths (triaxial, isotropic) and temperatures (from room temperature to over 800K).

We show that: 1) the mechanical response of sedimentary porous rocks at strains usually achieved in laboratory testing is determined by the the interface processes taking place at the cementitious material bonding the grains.; 2) this strength is stress path dependent; 3) the interfaces processes are shown to be important only when the deviatoric component of the loading is significant; and 4) including the energy and mass balance equations regularizes the numerical problem of localization of plastic deformation, offering an internal length scale to the mechanical problem.

Keywords:

---

1. Introduction

Constitutive modelling of irreversible deformation in geomaterials is currently transitioning from the design era to that of long-term modeling of processes. Such a transition requires a step-change in the models, not only designing structures up to their yield point but also capturing their behaviour beyond yield and offer predictive capabilities to long-term problems like the underground storage of energy waste, long-term energy production or seismic fault modeling. This requires a plasticity theory to help describe and even predict what is happening after yield, including far away from the initial yield at environments where rocks may experience extreme temperatures, pressures, but also internal transformations. To be able to model such multi-physical processes the constitutive models need to incorporate a sufficient

level of details from the physical mechanisms taking place at the microstructure, and which affect the macroscopic response of materials upon loading.

Examples of such models can be found in the field of Metal Plasticity, and in particular crystal plasticity with the first attempts of capturing the microscopic response of crystals date as early as the 1930s with the pioneering works of (Taylor and Quinney, 1934a; Eyring, 1936; Orowan, 1940; Kauzmann, 1941), to name but a few. Through these works it was shown -and nowadays it is commonly accepted- that the mechanical resistance in shear in metals is dominated by lattice-related processes like the presence of discrete obstacles, lattice resistance, dislocation movements, etc (for more details see (Frost and Ashby, 1982)).

Since metals are predominantly pressure insensitive (von Mises) materials, all these microstructural processes are affecting their shear response. They can all be up-scaled in the macroscopic expression of the (plastic) shear strain rate using concepts from statistical mechanics and chemical rate theory (see (Kauzmann, 1941) for example), to provide a viscous law of the form:

$$\dot{\gamma} = \dot{\gamma}_0 \left(\frac{\tau}{\tau_0} \right)^n e^{-\Delta Q/RT} \tag{1}$$

where τ is the shear stress and ΔQ is the activation enthalpy (increment) of the microscopic mechanisms, i.e. the energy that needs to be provided to overcome/activate any microstructural obstacles/mechanisms resisting the motion. It has been shown (Frost and Ashby, 1982) that this activation energy depends linearly on shear stress and can therefore be written as $Q = E - a\tau$. In cases where the microstructural mechanisms include pressure sensitivity and volume change, like for example lattice vacancies that are

filled, the activation enthalpy is extended to account for pressure sensitivity in the form $\Delta Q = \Delta E - \Delta a\tau + p\Delta V$ (see (Frost and Ashby, 1982), chapter 17).

These concepts have been cast into a visco-plastic framework by Perzyna (1966), Lubliner (1990) etc., regarding pressure-insensitive (i.e. exhibiting J2 or von-Mises yield) metals. They resulted into defining a flow law for plasticity as a similar function to Eq. (1):

$$\dot{\gamma}^p = \dot{\lambda}\frac{\partial y}{\partial \tau}, \dot{\lambda} = \dot{\gamma}_0 \langle \frac{\tau - \tau_0}{\tau_0} \rangle^n e^{-\Delta Q/RT} \tag{2}$$

where in this case, τ is the deviatoric stress, τ_0 is its value at yield and y is the von Mises yield surface ($\tau = \tau_0$). The addition of the macauley brackets $\langle . \rangle$ places these concepts into a plasticity framework, ensuring zero plastic strain rate before yield. The quantity $\tau - \tau_0$ inside the Macauley brackets is frequently called *overstress*, as it expresses the amount of stress in excess (over) of the current yield value that the material is experiencing. Based on this, this plasticity approach is usually called *overstress visco-plasticity*.

These concepts have been later generalized to apply in materials displaying pressure sensitivity and more complicated microstructures, like geomaterials (Oka, 1985, 1981; Adachi and OKA, 1982; Borja, 1991). Recently (Einav, 2012; Zhang and Buscarnera, 2017; Veveakis and Regenauer-Lieb, 2015) have extended these concepts to allow the flow law to receive feedback from state variables (including pressure,temperature and density). Such concepts are common knowledge in disciplines studying long-term response of rocks under loading, like Geology, Geophysics and Geodynamics, where the materials are long past their initial yield point and are commonly described

as viscous without incorporating the concept of a yield surface or plasticity in general (Karato, 2008). In these disciplines the viscosity of the material incorporates all the interface processes taking place at the micro-scale, like for example grain boundary sliding, interface chemistry etc. As such, the viscosity of these laws is expressing all the micro-scopic processes as a function of the state variables of the problem at hand, like temperature, pressure and density.

In this work, we suggest a Multiphysics Geomechanical framework that is enriched with a dependency of the plastic multiplier (viscosity) on state variables and internal interface processes. The next sections are laying down the fundamental principles of Continuum Mechanics used in the approach (mass, energy, local entropy and momentum balance), before developing and validating appropriate constitutive laws for the mechanical response of rocks experiencing internal interface mechanisms like debonding or interface dissolution/precipitation. The mathematical framework is then implemented in a finite element simulator and used to reproduce experimental results from triaxial and isotropic compression tests in different types of rocks. Finally, all the results are synthesized and novel conclusions discussed.

2. Mathematical Framework of Multi-Physics Mechanics

We start by presenting the governing laws of physics used in this framework. The work is based on the basic and fundamental principles of continuum mechanics, considering a representative elementary volume (REV), the smallest volume over which a measurement can be made that will yield a value representative of the whole (Hill, 1963). Given all applications in

this work involve rocks of a few centimetres at the smallest, this assumption is not restrictive for the type of rocks considered (mudstone, sandstone, carbonates).

2.1. Mixture's Theory

The continuum studied includes considerations for a two-phase material, made of a fully saturated porous matrix filled with fluid. As such, the material is decomposed into the part that constitutes the skeleton, receiving forces from the loading conditions, and the weak (or fluid) phase which occupies the void volume and does not participate into the force chain network. The volume ratio of the voids can therefore be defined as the porosity,

$$\phi = \frac{V_{void}}{V}, \tag{3}$$

which allows the deployment in the following sections of the well known governing equations for a bi-phasic material in the context of mixtures theory. Based on that, we then define the respective phase densities:

$$\rho_1 = (1 - \phi)\rho_s \tag{4a}$$

$$\rho_2 = \phi\, \rho_f \tag{4b}$$

where the subscripts s and f refer to the solid and fluid components respectively.

2.2. Mass Balance

The mass balance of the fluid and solid phases can be expressed as:

$$\begin{aligned} \frac{\partial \rho_1}{\partial t} + \frac{\partial (\rho_1 V_k^{(1)})}{\partial x_k} = 0 \\ \frac{\partial \rho_2}{\partial t} + \frac{\partial (\rho_2 V_k^{(2)})}{\partial x_k} = 0 \end{aligned} \tag{5}$$

In the case where the material is saturated with a fluid, each phase can assumed to follow the equation of the state with respect to the (state) pressure of the fluid p_f and Temperature T:

$$\frac{d\rho_{(i)}}{\rho_{(i)}} = \beta_{(i)} dp_f - \lambda_{(i)} dT, \quad i \in \{s, f\} \tag{6}$$

where $\beta_{(i)}$ is the compressibility ($\beta_{(i)} = \frac{1}{\rho_{(i)}} \left(\frac{d\rho_{(i)}}{dp_f} \right)_T$) and $\lambda_{(i)}$ is the thermal expansion ($\lambda_{(i)} = -\frac{1}{\rho_{(i)}} \left(\frac{d\rho_{(i)}}{dT} \right)_{p_f}$).

Using Eq. 5 and Eq. 6, combined with Darcy's law for the filter velocity $\phi(V_k^{(2)} - V_k^{(1)}) = -\frac{k}{\mu_f} \frac{\partial p_f}{\partial x_k}$ (k is the permeability an μ_f the saturating fuid viscosity) while neglecting convective terms, leads to the final mass balance equation for the mixture:

$$\beta_m \frac{\partial p_f}{\partial t} - \lambda_m \frac{\partial T}{\partial t} - \frac{k}{\mu_f} \frac{\partial^2 p_f}{\partial x_k x_k} + \frac{\partial V_k^{(1)}}{\partial x_k} = 0 \tag{7}$$

where $\beta_m = (1 - \phi)\beta_s + \phi\beta_f$ is the mixture's compressibility, and $\lambda_m = (1 - \phi)\lambda_s + \phi\lambda_f$ the mixture's thermal expansion coefficient.

2.3. Momentum Balance

The acceleration of the mixture is assumed to be negligible. Therefore, the local form of the momentum balance of the mixture together with Terzaghi's

law (Terzaghi, 1925) $\sigma_{ij} = \sigma'_{ij} - p_f \delta_{ij}$ (where σ_{ij} is the total stress tensor of the mixture, σ'_{ij} the effective stress tensor and p_f the pore pressure), can be written in its stress equilibrium regime as follows,

$$\frac{\partial \sigma'_{ij}}{\partial x_j} - \frac{\partial \Delta p_f \delta_{ij}}{\partial x_j} + b_i = 0 \tag{8}$$

By convention, stresses are taken negative in compression in this work. In this expression we decomposed the pore pressure itself as $p_f = p_{hyd} + \Delta p_f$ where p_{hyd} is the hydrostatic pressure (constant in this study) and Δp_f is the excess pore pressure.

2.4. Energy Balance

The local form of the energy equation expresses the energy balance and takes into account Fourier's law for heat conduction and the second law of thermodynamics (Rosakis et al., 2000):

$$(\rho C)_m \frac{\partial T}{\partial t} = \alpha \frac{\partial^2 T}{\partial x_i \partial x_i} + \Phi \tag{9}$$

where $(\rho C)_m$ the heat capacity of the mixture and α the thermal conductivity. The term Φ corresponds to the mechanical work dissipated into heat, which is non negative based on the second law of thermodynamics:

$$\Phi = \sigma'_{ij} \dot{\epsilon}^i_{ij} + \frac{\partial \psi}{\partial \xi_k} \dot{\xi}_k \geq 0 \tag{10}$$

In this expression, the (frequently called cold-) work of internal state variables is expressed through the product of derivative of the Helmholtz free energy ψ with respect to any dissipative internal state variable vector ξ_k and its rate, $\frac{\partial \psi}{\partial \xi} \dot{\xi}_k$. The expression (10) can be re-arranged to take the form:

$$\Phi = \chi \sigma'_{ij} \dot{\epsilon}^i_{ij} \geq 0 \, , \; \chi = 1 - \frac{E_\xi \dot{\xi}_k}{\sigma'_{ij} \dot{\epsilon}^i_{ij}} \tag{11}$$

where $E_\xi = -\frac{\partial \psi}{\partial \xi_k}$ and χ is the Taylor-Quinney coefficient (Taylor and Quinney, 1934b), expressing the amount of mechanical work dissipated by the internal state variables into internal microstructural mechanisms. When it is zero all the mechanical work is consumed into internal state variables, whereas when it is equal to one all the mechanical work is converted into heat. χ is in general a function of all the state variables, like density (or pressure), temperature, ξ_k, etc.

2.5. Normalisation

The assessment of the influence of the various physical processes involved, is facilitated by adopting a dimensionless formulation. To that end, the following normalised variables are introduced:

$$p^* = \frac{p_f}{\sigma_{ref}}, \tag{12a}$$

$$T^* = \frac{T - T_{ref}}{T_{ref}}, \tag{12b}$$

$$x^* = \frac{x}{x_{ref}}, \tag{12c}$$

$$t^* = \frac{c_{th,ref}}{x_{ref}^2} t. \tag{12d}$$

where $c_{th,ref} = \alpha_{th} / \left(\rho C_p\right)_m$ is a reference thermal diffusivity of the mixture, with α_{th} the thermal conductivity and ρC_p the heat capacity of the mixture.

By introducing those normalized numbers to equation 7, we obtain (the asterisks are dropped for simplicity.):

$$\frac{\partial \Delta p_f}{\partial t} - \frac{\partial}{\partial x_k}\left[\frac{1}{Le}\frac{\partial \Delta p_f}{\partial x_k}\right] - \Lambda_m \frac{\partial T}{\partial t} + \frac{\dot{\epsilon_V}}{\bar{\beta}} = 0 \tag{13}$$

where $\Lambda_m = \frac{\lambda_m T_{ref}}{\beta_m \sigma_{ref}}$ is the thermal pressurization coefficient for mixture, Pe is

Péclet number, $\bar{\beta} = \beta_m \sigma_{ref}$ is the normalized compressibility of the mixture and $\dot{\epsilon_V}$ is the normalized volumetric strain rate.

Following the same procedure, the energy balance is brought in a dimensionless form:

$$\frac{\partial T}{\partial t} - \frac{\partial^2 T}{\partial x_k \partial x_x} - Gr\ \sigma_{ij} \dot{\epsilon}_{ij}^{pl} = 0 \tag{14}$$

where $Gr = \frac{\sigma_{ref} \dot{e}psilon_{ref} x_{ref}^2}{\alpha_{th} T_{ref}}$ is a dimensionless group called the Gruntfest number (**?**).

These 2 equations, together with the normalised form of the stress equilibrium (gravity is neglected in the following), are constituting the final system of equations. These three equations are closed as a mathematical system when appropriate constitutive laws of elasto-plasticity are taken under considerations. Since in this study we are interested in studying materials with internal interfacial mechanisms taking place during irreversible deformation, the next section is devoted into the development and validation of such constitutive expressions.

3. Constitutive Laws of Multi-Physics Elasto-Visco-Plasticity

In this section we describe the temperature- and pressure- sensitive law of elasto-viscoplasticity. The underlying physical model for this study is combining concepts from the viscoplastic approach in metals, as discussed in the introduction, with the required modifications to capture interface mechanisms in pressure-sensitive, porous materials.

3.1. Elasto-Visco-Plasticity

The formulation is based on the principles of overstress plasticity (Perzyna, 1966), used in a novel elasto-viscoplastic approach Poulet and Veveakis (2016). As is done classically in Mechanics, the total strain rate is decomposed into its elastic (reversible) and plastic (irreversible) components, $\dot{\epsilon}_{ij} = \dot{\epsilon}^r_{ij} + \dot{\epsilon}^i_{ij}$.

3.1.1. Thermo-Poro-Elasticity

The reversible part is considered to observe linear thermo-elasticity,

$$\dot{\epsilon}^r_{ij} = C_{ijkl}\dot{\sigma}'_{kl} - \lambda_s \Delta T \tag{15}$$

where C_{ijkl} is the compliance modulus. Note that the Einstein notation (summation of repeated indices) applies.

3.1.2. Visco-plasticity

The irreversible element of the strain rate respects an associative visco-plastic flow law expressed as $\dot{\epsilon}^i_{ij} = \dot{\Pi}\frac{\partial f}{\partial \sigma'_{ij}}$, where f is the yield function and $\dot{\Pi}$ is a (scalar) plastic multiplier (see figure 1).

The plastic multiplier is chosen as the norm of the tensor, obeying the relation $\dot{\Pi} = \sqrt{\dot{\epsilon}^{i\,2}_d + \dot{\epsilon}^{i\,2}_v}$, where $\dot{\epsilon}^i_d$ and $\dot{\epsilon}^i_v$ represent the deviatoric (i.e. irreversible processes occuring in the absence of volume change) and volumetric (i.e. irreversible processes occuring in the absence of shear) components of the strain rate tensor respectively (see figure 1), obeying the incremental relations:

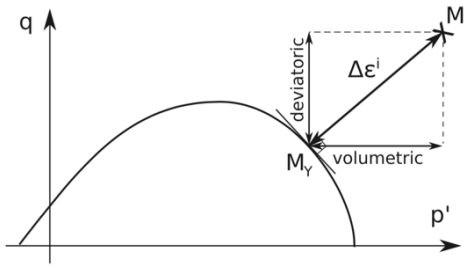

Figure 1: Decomposition of the plastic flow rule into a volumetric and a deviatoric components in the $p' - q$ space (mean effective stress shear stress), for a stress point M and its corresponding point on the yield point M_Y.

$$\dot{\epsilon}_d^i = \dot{\epsilon}_0^d \left\langle \frac{q - q_Y}{\sigma_{ref}} \right\rangle^m, \tag{16a}$$

$$\dot{\epsilon}_v^i = \dot{\epsilon}_0^v \left\langle \frac{p' - p_Y}{\sigma_{ref}} \right\rangle^m, \tag{16b}$$

where $\dot{\epsilon}_0^{v,d}$ is the reference strain rate for the deviatoric and volumetric part, p' denotes the volumetric mean effective stress, q the equivalent deviatoric stress (also called von Mises stress), p_Y and q_Y the corresponding values of p' and q at yield, R the universal gas constant, σ_{ref} a reference value to normalize stresses, and T the temperature. The angle brackets $\langle \cdot \rangle$ represent Macaulay brackets.

Following the discussion in the Introduction, the reference strain rates are assumed to take Arrhenius-like forms like:

$$\dot{\epsilon}_0^d = \dot{\epsilon}_0 \exp\left(-\frac{\Delta Q_{mech}^d}{RT}\right), \tag{17a}$$

$$\dot{\epsilon}_0^v = \dot{\epsilon}_0 \exp\left(-\frac{\Delta Q_{mech}^v}{RT}\right) \tag{17b}$$

where ΔQ^d_{mech} and ΔQ^v_{mech} are the activation enthalpies of the deviatoric and volumetric components, expressing the activation energy required to overcome (activate) the dissipative mechanisms admissible by the microstructure. The enthalpies are functions of all the state variables of the problem (density, pressure, temperature, etc). Therefore, temperature, pressure and density dependencies are accounted for through the definition of the activation enthalpies for the deviatoric (ΔQ^d_{mech}) and the volumetric (ΔQ^v_{mech}) components of the irreversible strain rate. Those terms incorporate the activation energies of all micromechanical mechanisms taking place, including frictional initiation (Rice et al., 2001), volumetric pore collapse (Poulet and Veveakis, 2016), or debonding and grain cracking (Zhang and Buscarnera, 2017), and can be functions of all the global and internal state variables of the problem at hand. In essence, these exponential expressions are used in this framework as mechanisms to replace the hardening laws of classical plasticity. An example of such an approach is illustrated in the following section for arbitrary processes at the skeleton's interface, emphasizing the specific mechanism of debonding in an isotropic medium where $\Delta Q^d_{mech} = \Delta Q^v_{mech} = \Delta Q_{mech}$. Through considerations of the interface physics at the grain scale, we are able to upscale for a continuum expression of ΔQ_{mech} in the considered REV.

3.2. Interface Laws for Debonding Processes at the Grain Scale

Let us consider a generic system of two grains submerged in a saturating fluid, and assume them being connected through a bonding interface which can be of solid (cement) or fluid (capillary bridge) form. This system of grains and bond (skeleton) is experiencing a mean pressure P_{sk}, while the saturating fluid is experiencing a mean pressure p_f. In such a system,

debonding/bonding processes may take place at the interface, with them being of chemical (dissolution/precipitation) or mechanical (breakage/healing) origin, or even a combination thereof (e.g. breakage/precipitation or dissolution/healing). A generic way of approaching this interface configuration, is to assume that the interface is allowed to experience a transition of the solid skeleton into a fluid (and vice versa), following a phase transformation of the form $skeleton \rightleftharpoons fluid$. Since all these processes -irrespectively of their origin- are affecting the mechanical response of the skeleton, the activation enthalpy of the mechanical law needs to account for these interface effects. In a two-grain (single contact) system, this is expressed in incremental form as:

$$\Delta q_{mech} = \Delta q^0_{mech} + \Delta q_{interface} = \Delta q^0_{mech} + \sum_i \mu_i \Delta m_i \tag{18}$$

In this equation Δq^0_{mech} is the base enthalpy of the system and $\Delta q_{interface} = \sum_i \mu_i \Delta m_i$ for $i = sk, f$ is the enthalpy of the interface, expressing the energy required to break chemo-mechanical bonds of the skeleton and form weak fluidized phases. μ_i is the chemical potential and m_i the mass of each constituent.

The mechanical enthalpy of a system of multiple contacts is obtained if we average Eq. (18) over the volume of our Representative Elementary Volume (REV) V for a given contact distribution $N(V)$:

$$\Delta Q_{mech} = \frac{1}{V} \int \Delta q_{mech} N(V) dV \tag{19}$$

For the simple case of a uniform contact distribution we obtain:

$$\Delta Q_{mech} = \Delta Q^0_{mech} + \mu_1 \Delta \rho_1 + \mu_2 \Delta \rho_2 \tag{20}$$

where $\Delta Q^0_{mech} = \Delta q_{mech} n_c$, with n_c being the number of evenly distributed contacts in the REV. The indices $1, 2$ are referring to the solid and fluid phases, respectively ($\mu_1 = \mu_{sk} n_c$, $\mu_2 = \mu_f n_c$). Note that all the contacts are assumed energetically equiprobable, allowing for the chemical potentials to be considered constant over the volume averaging procedure. Substituting in Eq. (20) the mixture's expressions for the densities $\rho_1 = (1 - \phi)\rho_{sk}$ and $\rho_2 = \phi \rho_f$, with ϕ being the porosity of the mixture, we obtain:

$$\Delta Q_{mech} = \Delta Q^0_{mech} + \left(\mu_f n_c \rho_f - \mu_{sk} n_c \rho_{sk}\right) \Delta \phi \tag{21}$$

Note that when the two phases of the interface are in equilibrium, the chemical potentials are equal, $\mu_f = \mu_{sk}$.

Recalling the Equation of State (EoS) considered (Eq. 6), we may express $\Delta\phi$ in terms of the excess pore fluid pressure and temperature variation, $\Delta \phi = \phi_0 \beta_\phi \Delta p_f - \phi_0 \lambda_\phi \Delta T$, where β_ϕ, λ_ϕ are the compressibility and thermal expansion coefficients of the void space Rice (2006). In addition, the chemical potentials of the $i-$species are frequently expressed through their partial pressures experienced, through a pressure-like quantity f Karato (2008):

$$\mu_i = \mu_0 + RT \ln \frac{f_i}{f_0} \tag{22}$$

where μ_0 is a reference value of the chemical potential at a reference value f_0, that will be set to zero hereafter to ensure tractability of the mathematical derivations. The pressure-like quantity f is identified as the fugacity in the case of gaseous constitutents. It has the units of pressure and is an "effective

pressure" i.e, the pressure that gives the correct value for the chemical potential of a real gas. In case of ideal gases, the fugacity is therefore equal to the gas pressure P. In the more general case of condensed (liquid or solid) phase, the deviation of the fugacity from the ideal case is expressed through a fugacity coefficient ν linking it to a representative pressure of the system for each constituent i, $f_i = \nu_i P$ (Karato, 2008). In this case the reference value is set to $f_0 = P$.

Substituting the above considerations into Eq. (21) we finally obtain:

$$\Delta Q_{mech} = \Delta Q^0_{mech} + \frac{\phi_0}{\rho_0} n_c \beta_\phi RT \left(\rho_f \ln \nu_f - \rho_{sk} \ln \nu_{sk}\right) \left(\Delta p_f - \frac{\lambda_\phi}{\beta_\phi} \Delta T\right) \quad (23)$$

Since the fugacity coefficients are in principle unknown for non-ideal gas components, in this study they will be first used as inversion parameters, and later discussed for their physical origin and applicability to the mechanics of sedimentary rocks. We will therefore be using the following expression,

$$\Delta Q_{mech} = \Delta Q^0_{mech} + \Delta p_f V_{act} \quad (24)$$

where $V_{act} = \frac{\phi_0}{\rho_0} \beta_\phi n_c \left(\rho_f \ln \nu_f - \rho_{sk} \ln \nu_{sk}\right) RT$, and we assumed for simplicity that the void space has negligible thermal expansion coefficient compared to its compressibility, so that $\frac{\lambda_\phi}{\beta_\phi} \to 0$.

3.3. Model Validation Against Varying Temperature and Pressure for Different Rocks

In this section we calibrate the visco-plastic constitutive law for different pore pressures and temperatures and restrict further the mathematical formula of the chosen Arrhenius law of Eqs. (17), which encapsulates the

pressure and temperature sensitivity of the model. For this task, the experimental data from Fischer and Paterson (1989) have been chosen, comprising a series of triaxial tests in Carrara marble, Solnhofen limestone and Gosford sandstone. These tests were performed under constant confinement (300 MPa), and the pore pressure was used to vary the mean effective stress instead of directly controlling the confining pressure as in typical triaxial experiments. Five different values of the pore pressure were applied, ranging from 30 to 280 MPa. Furthermore, the experiments were conducted at four different values of temperature ($20° - 600°$C), and two loading rates ($10^{-4}s^{-1}$ and $10^{-5}s^{-1}$). An example of the results reported can be found in figure 9a of Fischer and Paterson (1989).

Given the number of possible combinations of these tests, Fischer and Paterson focused on reporting mainly the axial stress of the material at 10% axial strain as representative deformation at post yield state of the material (as can be seen figure 9b in (Fischer and Paterson, 1989)). At this strain the materials are already in the post-yield regime, having accumulated significant plastic deformation. Since our target in this session is to calibrate the viscoplastic formulation against these data, the following simplifying assumptions have been made based on the experimental results: 1) the material is treated as rigid-viscoplastic, 2) the material admits a Drucker-Prager yield surface. This choice allows to properly describe the pressure sensitivity of the material as suggested by the experimental data while keeping the yield surface as simple linear relationship ($F_y = 0$) (as can be seen in figure 9a,b in (Fischer and Paterson, 1989)).

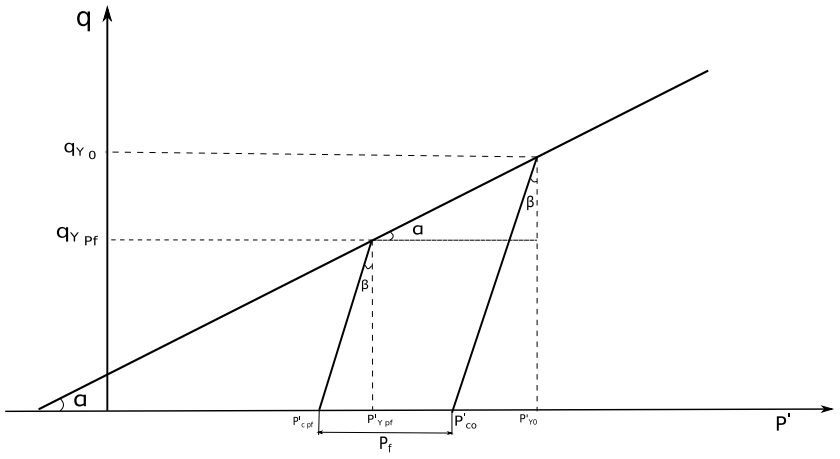

Figure 2: Schematic of the flow law, drawn in a compression positive sign convention for simplicity

3.3.1. Equations for fitting drained triaxial experimental data

Using this assumptions, our goal is to capture the non-linearity of the post-yield response using only the proposed overstress constitutive law, starting from the deviatoric expression of the flow law,

$$\dot{\epsilon}_{vp} = \dot{\epsilon}_{ref} \left\langle \frac{q - q_Y}{q_Y} \right\rangle^m \exp\left(-\frac{\Delta Q_{mech}}{RT}\right) \tag{25}$$

where as a first approach we assume that the activation enthalpy is obeying the isotropic law of Eq. 24: $\Delta Q_{mech} = \Delta E + \Delta p_f V_{act}$.

By inverting Eq. 25 for the deviatoric stress q, assuming that the loading is monotonous, we obtain:

$$q = q_Y \left[1 + A \exp\left(\frac{\Delta E + \Delta p_f V_{act}}{mRT}\right)\right] \tag{26}$$

where $A = (\frac{\dot{\epsilon}^i_{vp}}{\dot{\epsilon}_{ref}})^{1/m}$.

The experiments of Fischer and Paterson (1989) follow the standard stress path of drained triaxial tests. Let the subscript 0 denote the dry material,

which is under the maximum effective confining pressure applied (300MPa) and the subscript p_f denote any other state where some constant pore pressure is applied. Then, following the sketch in Figure (2) we can define a ratio of stresses based on the stress path,

$$\tan\beta = \frac{p'_{y(pf)} - p'_{c(p_f)}}{q_{y(p_f)}} = \frac{p'_{y(0)} - p'_{c(0)}}{q_{y(0)}} = \frac{1}{3} \tag{27}$$

Solving for the mean effective stress, we obtain:

$$p'_{y(p_f)} = p'_{c(p_f)} + \frac{1}{3} q_{y(p_f)}, \tag{28a}$$

$$p'_{y(0)} = p'_{c(0)} + \frac{1}{3} q_{y(0)}, \tag{28b}$$

The pore pressure p_f can be calculated as $p_f = p'_{c(0)} - p'_{c(p_f)}$. By substituting the latter in equation (28a) we derive

$$p'_{y(0)} - p'_{y(p_f)} = \frac{1}{3}\left(q_{y(0)} - q_{y(p_f)}\right) + p_f \tag{29}$$

Also, from the graphical definition of the friction angle α we obtain:

$$\tan\alpha = \frac{q_{y(0)} - q_{y(p_f)}}{p'_{y(0)} - p'_{y(p_f)}} \tag{30}$$

which in turn yields:

$$q_{y(p_f)} = q_{y(0)} - p_f \left(\frac{3\tan\alpha}{3 - \tan\alpha}\right). \tag{31}$$

By substituting equation (31) in equation (26), we arrive at the final equation that will be used to invert for the material properties of the model:

$$q_{fit} = \left(q_{y(0)} - p_f \left(\frac{3\tan\alpha}{3-\tan\alpha} \right) \right) \left(1 + A \exp\left(\frac{E + p_f V_{act}}{mRT} \right) \right) \tag{32}$$

In order to model the experimental data for those three types of materials (sandstone, limestone and marble) equation (32) is then used to invert for q_{fit} by using the following as inversion parameters: 1) the friction angle of the yield surface, α 2) $A = (\frac{\dot{\epsilon}^i_{vp}}{\dot{\epsilon}_{ref}})$, 3) the activation energy $\Delta E/m$ and 4) the activation volume V_{act}. Note that out of all these parameters the activation volume is the most poorly constrained.

3.3.2. Parameter inversion from drained triaxial experimental data

Starting with the sandstone data (figure 3a,b) it is observed that the material remains pressure sensitive throughout the experiments and the results are fairly regular. As such, it seems reasonable to assume that the composition of the material remains the same despite the significant increase in the temperature. For this series of data, the inversion was made with respect to the activation volume, while searching for the optimal values of the friction angle the strain rate ratio and the activation energy. The values used to fit the data at $10^{-4}s^{-1}$ and $10^{-5}s^{-1}$ strain rate are summarized in tables (1) and (2) respectively.

The corresponding results of the calibration are shown in figure (3a,b). Note that the nature of the activation volume is unknown in the thermo-mechanical context at the laboratory scale so far, and as such it is used as a free parameter inverted from the fitting exercise. Significant variation in V_{act} could be explained as the result of the debonding of grains for instance. Note that the change of the parameter A from 0.5 to 0.2 at $10^{-4}s^{-1}$ and

Strain Rate$10^{-4}s^{-1}$					
$T(K)$	$q_y(MPa)$	α	A	$\Delta E/m(J/mol)$	$V_{act}(J/Pa.mol)$
293	340	35°	0.5	1390	-0.001816
473	340	35°	0.5	1390	-0.001235
673	340	35°	0.5	1390	-0.00254
873	340	35°	0.5	1390	-0.004898

Table 1: Parameters used to fit experimental data for sandstone at $10^{-4}s^{-1}$ strain rate

Strain Rate$10^{-5}s^{-1}$					
$T(K)$	$q_y(MPa)$	α	A	$\Delta E/m(J/mol)$	$V_{act}(J/Pa/mol)$
293	380	40.11°	0.2	2936	-8.86e-14
473	380	40.11°	0.2	2936	-4.02e-12
673	380	40.11°	0.2	2936	-7.072e-13
873	380	40.11°	0.2	2936	-0.01349

Table 2: Parameters used to fit experimental data for sandstone at $10^{-5}s^{-1}$ strain rate

$10^{-5}s^{-1}$ strain rate, respectively represents the viscous effect triggered from the change in the loading rate.

By looking at the reported data of limestone and marble (Fig. 4a,b and 5), it can be observed that the pressure sensitivity changes significantly with increasing the temperature. The materials become more pressure insensitive (i.e. undrained), indicative of excess pore pressure generation inside the sample. A possible candidate for a mechanism causing excess pore pressure under high temperatures in carbonate-rich rocks is the presence of a fluid-release

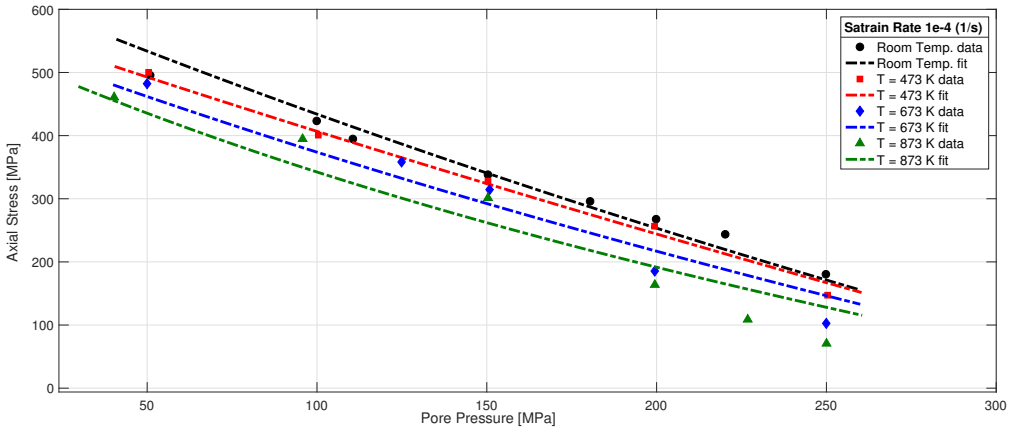

(a)

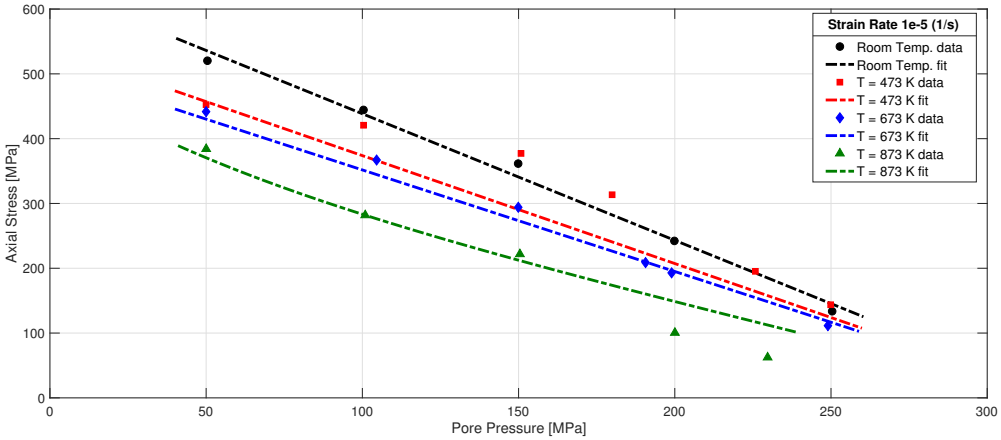

(b)

Figure 3: (a) Fitting sandstone data at $10^{-4}s^{-1}$ strain rate, (b) Fitting sandstone data at $10^{-5}s^{-1}$ strain rate

chemical alteration, potentially producing excess pore fluid pressure during chemical decomposition. This chemical change has been reported by Fischer and Paterson (1989), who stated that the limestone material was uncontrollable at high temperature and higher strain rate. The chemical alteration leads to the change of the yield surface, decreasing the friction angle α and the viscosity as expressed by the ratio of strain rates A. Therefore, in the optimization process those two parameters were allowed to vary for each temperature to capture the behaviour for limestone and marble, while V_{act} and E/m were kept constant. Setting the value of V_{act} at very low values renders the hydraulic effects inactive, which seems reasonable since the experiments are drained and the pressure sensitivity is negligible at high temperatures.

Strain Rate$10^{-4}s^{-1}$					
$T(K)$	$q_y(MPa)$	α	A	$\Delta E/m(J/mol)$	$V_{act}(J/Pa/mol)$
293	61.55	6.674°	0.04737	1000	-1.274e-11
473	61.55	4.049°	0.2606	1000	-1.274e-11
673	61.55	0.4929°	0.4536	1000	-1.274e-11
873	61.55	0.8898°	0.3181	1000	-1.274e-11

Table 3: Parameters used to fit experimental data for limestone at $10^{-4}s^{-1}$ strain rate

The values used to fit the limestone data at $10^{-4}s^{-1}$ and $10^{-5}s^{-1}$ strain rates are summarized in tables (3) and (4), respectively. The corresponding results of the calibration are presented in figure (4a,b). Finally, the values used to fit the data for marble at $10^{-4}s^{-1}$ strain rate are summarized in table (5), and the corresponding results of the calibration can be found in figures (5).

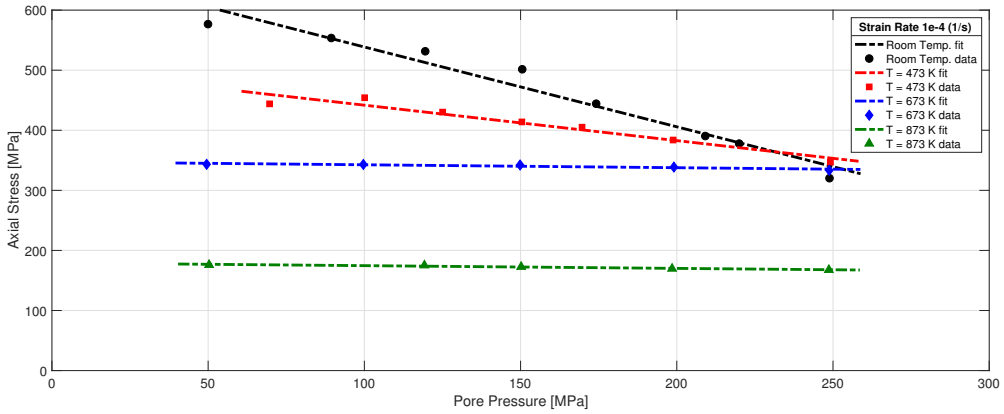

(a)

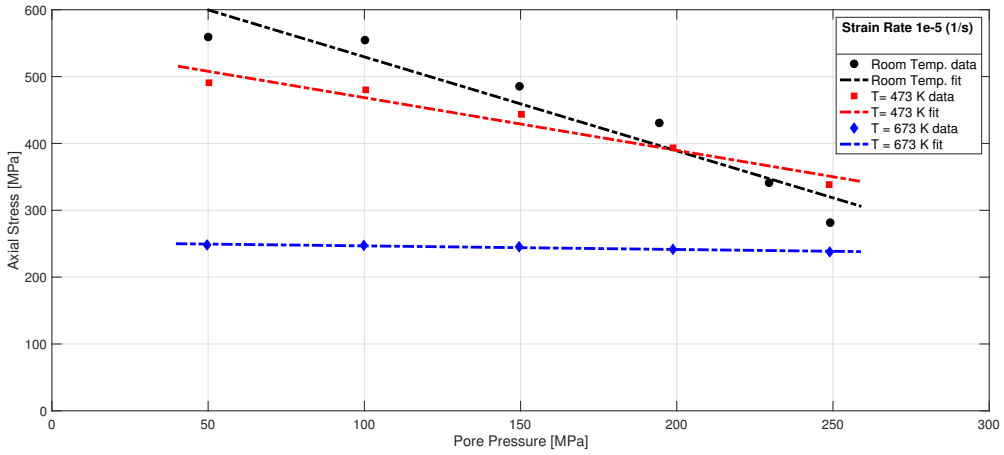

(b)

Figure 4: (a) Fitting limestone data at $10^{-4}s^{-1}$ strain rate, (b) Fitting limestone data at $10^{-5}s^{-1}$ strain rate

Strain Rate$10^{-5}s^{-1}$					
$T(K)$	$q_y(MPa)$	α	A	$\Delta E/m(J/mol)$	$V_{act}(J/Pa/mol)$
293	110	12.1°	3.376	1000	-3.916e-14
473	110	8.562°	3.083	1000	-3.916e-14
673	110	1.334°	1.081	1000	-3.916e-14

Table 4: Parameters used to fit experimental data for limestone at $10^{-5}s^{-1}$ strain rate

Strain Rate$10^{-4}s^{-1}$					
$T(K)$	$q_y(MPa)$	α	A	$\Delta E/m(J/mol)$	$V_{act}(J/Pa/mol)$
293	153	17.6°	1.554	1000	-1.333e-11
473	153	11.64°	1.273	1000	-1.333e-11
673	153	10.39°	0.9774	1000	-1.333e-11
873	153	7.093°	0.01495	1000	-1.333e-11

Table 5: Parameters used to fit experimental data for marble at $10^{-4}s^{-1}$ strain rate

In summary, all calibrations in this section show that the model can capture adequately the rate, temperature, and pressure dependency of different materials. They can be included just by changing the yield surface as in classical thermo-plasticity. The assumptions used here are crude as in the lab scale, thermo-elastic effects are important. The fact that the model does a good job despite that should be noted here. However, the fact that the same model, with reasonable and comparable parameter values, can capture adequately the behaviour of a variety of materials at different temperature and pressure conditions, suggests that this model is sufficiently rich to be

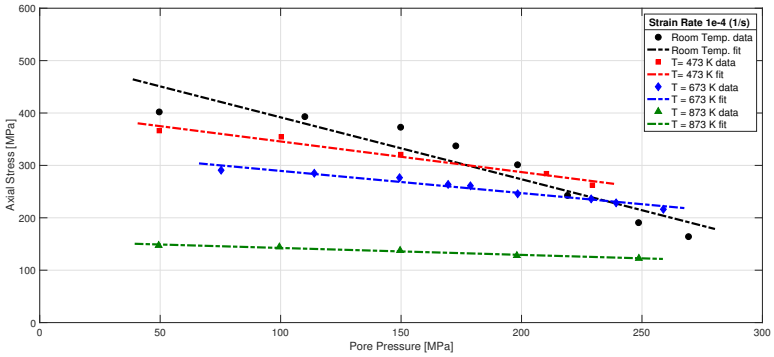

Figure 5: Fitting marble data at $10^{-4}s^{-1}$ strain rate

used across materials and loading conditions.

4. Numerical Implementation and Behaviour of the Framework

This section presents the numerical approach used to solve the theoretical framework described previously using REDBACK, an open-source parallel simulator for Rock mEchanics with Dissipative feedBACKs (Poulet and Veveakis, 2016). An indicative suite of benchmarks is also reported to test some of the key capabilities of the model. In particular we are showing the model's response: 1) in isotropic compression, retrieving the slope of virgin consolidation and over-consolidation cases, as well as performing velocity steps; 2) in cyclic isotropic compression, to show how isotropic hardening ensures appropriate cyclic response of the model; 3) in simple shear, to show that considering the energy equation provides an internal length scale that regularizes the localization problem during softening of the material; 4) in biaxial loading, to show the progressive localization of plastic deformation stemming from the multi-physical feedbacks.

4.1. REDBACK: A Parallel Finite Element Simulator

The complexity of the model presented previously makes it necessary to employ adequate numerical methods to solve the system of equations presented in section 2. The main challenge is the tight coupling between all variables in those equations - displacement $u_i(u_x, u_y, u_z)$, pore pressure and temperature - as well as the highly non-linear evolution of material properties such as porosity and permeability. As such, the traditional solving of all equations sequentially can lead to insurmountable numerical instabilities and convergence issues (Poulet et al., 2012).

Considering the continuum scale of the mechanical problem and the non-linearity of the feedbacks points to the Finite Element Method as an appropriate technique to solve that problem. The Multi-physics Object Oriented Simulation Environment MOOSE (Gaston et al., 2009) provides the flexibility to code very rapidly and investigate more complex physics implicitly, in a tightly coupled manner, therefore accounting accurately for nonlinear feedbacks. It also provides the computational scalability to simulate large 3D scenarios using High Perfomance Computing facilities. Specifically, the REDBACK simulator (Poulet and Veveakis, 2016) is an application based on MOOSE which was designed exactly for the purpose of solving the type of THMC systems that described previously, expressed in dimensionless form to properly account for the relative importance of the various physical processes.

4.2. Overstress Plasticity Return Map Algorithm

Within the final system of equations equations (8, 13, 14), the momentum balance plays a particular role as its corresponding variables (displacement

$u_i(u_x, u_y, u_z)$) are not representated explicitly, but through the stress divergence. It is the role of the return map algorithm to compute the value of stress for a given displacement (Poulet and Veveakis, 2016). The main algorithm is briefly summarized here to show explicitly the links between the theoretical model and the numerical implementation.

The displacement (u_i) is firstly converted to strain (ϵ_{ij}) using a finite strain approach (Rashid, 1993) and an overstress plasticity formulation implemented following the generic approach from Wang (Wang et al., 1997) to update the stress by using a fully implicit integration scheme as shown in figure (1).This algorithm uses a Newton-Raphson loop to find the values of the plastic strain rate and stress satisfying the selected flow law. Figure 1 shows the central importance of the flow law in the resolution of the mechanical problem and highlights the choice in this study of working on the formulation of that flow law to integrate multi-physical processes.

4.3. Simple Shear: Regularising the Post-Bifurcation Regime

Geomaterials exhibit a spontaneous change of the deformation mode from uniform deformation towards either diffuse or localized failure patterns in the inelastic regime (see (Vardoulakis and Sulem, 1995) for a comprehensive summary of the main results on this topic). Within the framework of bifurcation theory, this phenomenon can be modelled as a mathematical instability and, given an elasto-plastic constitutive law with a non-associative flow rule, it was shown that its onset can occur either in the strain hardening or in the strain softening regime (Rudnicki and Rice, 1975). As such, predicting a finite thickness of localization bands (Muhlhaus and Vardoulakis, 1987) is a necessary feature of any model designed to describe the inelastic behaviour

Compute elastic guess $\sigma_{ij}^{g} = \sigma_{ij}^{t} + E_{ijkl}\Delta\epsilon^{t+\Delta t}$

if $f(\sigma_{ij}^{g}) \geq 0$ *(plasticity)* **then**

  $\Delta\lambda^{(m=0)} = 0$

  $\sigma_{ij}^{(t+\Delta t, m=0)} = \sigma_{ij}^{(t)} + E_{ijkl}\left(\Delta\epsilon_{kl} - \Delta\lambda^{(m=0)}\frac{\partial f}{\partial\sigma_{kl}}\right)$

  $r^{(m=0)} = \Pi\left(\sigma_{ij}^{(t+\Delta t, m=0)}\right) - \frac{\Delta\lambda^{(m=0)}}{\Delta t}$

  while $|r| \geq tolerance$ **do**

    Compute yield values $p_Y^{(m+1)}$ and $q_Y^{(m+1)}$

    Compute flow increment $\frac{\partial f}{\partial\sigma_{ij}}^{(m+1)}$

    Compute plastic multiplier $\delta\lambda$ from jacobian of residual with respect to stress

    $\Delta\lambda^{(m+1)} = \Delta\lambda^{(m)} + \delta\lambda$

    $\sigma_{ij}^{(t+\Delta t, m+1)} = \sigma_{ij}^{(t)} + E_{ijkl}\left(\Delta\epsilon_{kl} - \Delta\lambda^{(m+1)}\frac{\partial f}{\partial\sigma_{kl}}\right)$

    $r^{(m+1)} = \Pi\left(\sigma_{ij}^{(t+\Delta t, m+1)}\right) - \frac{\Delta\lambda^{(m+1)}}{\Delta t}$

  end

else

  $\sigma_{ij}^{t+\Delta t} = \sigma_{ij}^{g}$

end

=

Figure 6: Return mapping routine used to compute a stress value at a given time step of the simulation. See (Poulet and Veveakis, 2016) for details.

of geomaterials (see also Sulem et al., 2011; Veveakis et al., 2012, 2013; Rattez et al., 2017, 2018a,b). As shown by (Needleman, 1988), the combination of the momentum balance law and the rheology of a viscous material under simple shear fails to provide a finite thickness at the quasi-static limit of the equations. In such a case, the latter is equal to the size of a predetermined imperfection, contradicting the concept that localization stems from the constitutive description of the material and is a material property. Indeed, when neglecting the energy and mass balance laws, it is only by introducing inertia terms in the momentum balance law that one can "regularise" the problem of shear banding for a rate-dependent material by delaying its arrival to the stationary wave limit, as shown by (Sluys, 1992). That study also showed that the shear band thickness l for a rate-dependent J2- material following a Perzyna-type law can be calculated as:

$$l = \frac{4\sigma_Y c_s}{3\gamma E} \tag{33}$$

where γ is the reference shear strain rate of the material, E is the Young's modulus, $c_s = \sqrt{G/\rho}$ is the elastic shear wave speed velocity (G is the elasticity shear modulus and ρ is the density of the material). Using the formulation equation (17a), $\gamma = \dot{\epsilon}_0 \exp\left(-Q^d_{mech}/RT\right)$ and therefore

$$l \propto \exp\left(\frac{Q^d_{mech}}{RT}\right) \tag{34}$$

One question that remains is whether including the remaining basic principles of Continuum Mechanics, i.e. the energy and mass balance laws, the length scales associated with these laws can extend the suitability of rate-dependent models to the quasi-static case as suggested by (Paesold et al.,

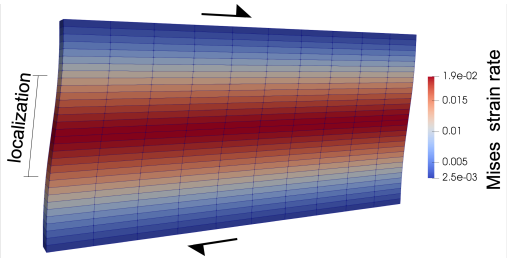

Figure 7: Simple shear of a von Mises material. Constant temperature and velocity boundary conditions were used.

2016). In particular, whether adopting a thermoplastic flow rule similar to equation (17a) and including the temperature diffusion equation (9), is sufficient for regularising the problem in the quasi-static case.

To answer this question, we consider the problem of simple shear of a layer with isothermal and constant velocity boundary conditions (see Figure 7). The material obeys the visco-plastic flow rule of equation (17a) with a von Mises yield function. The equations are discretised and solved using the REDBACK simulator. As shown in Figure (8a), after a short-lived strain hardening regime, the material enters a softening phase and subsequently reaches a constant-stress residual state. This behaviour is driven by the evolution of temperature, which, as can seen in Figure (8b), increases because of shear heating and then stabilises to a residual state clearly associated with the heat diffusion process. After 1% plastic stain, both the temperature and stress profiled have equilibrated.

Figure (9a) presents a mesh sensitivity analysis by varying the number of elements across the layer and plotting the corresponding profile of deviatoric strain rate. The results show that convergence is reached for 16 elements to a profile of localised deformation around the center of the layer. The thickness

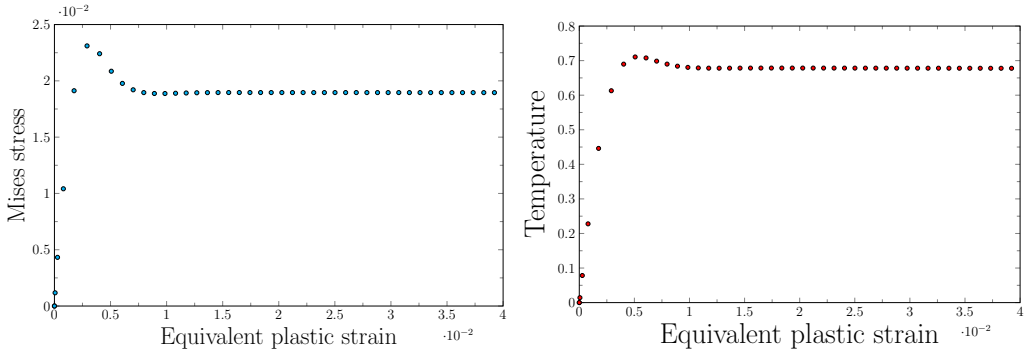

(a) (b)

Figure 8: a) Deviatoric stress at the core of the sample and b) normalized core temperature vs plastic shear strain. At first, the material appears to be in softening due to the temperature increase induced by shear heating until it reaches a residual regime. Notice that the shear band thickness is measured at this residual regime.

of localisation, which is mesh insensitive (see figure (9a)), is computed as the distance between the inflection points of the shear strain rate profile and plotted in figure (9b) for different values of the activation enthalpy Q_{mech} (normalised by the boundary temperature). The results show that we retrieve the exponential dependency of the localisation thickness on the Q_{mech} of equation 34.

4.4. Biaxial loading: Progressive Thermo-Mechanical Localization

A key feature of the presented framework is that localization is not spontaneous. Rather than that, deformation is progressively localizing, following the time-scales of the diffusion-reaction equations of temperature and/or pore-pressure. To demonstrate this, we summarize in Fig. 10 the results of a biaxial experiment (displacement controlled axial load, constant confinement on the sides, zero displacement on the out-of-page direction) performed at a

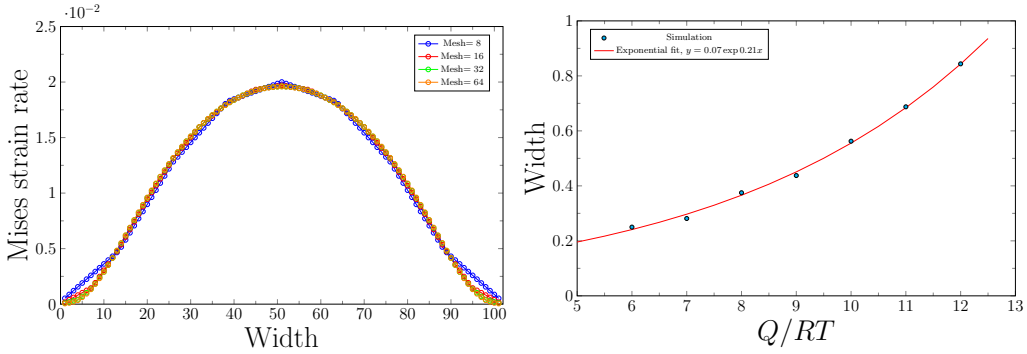

(a) (b)

Figure 9: (a) Profile of temperature at the residual state for different number of finite elements ($horizontal \times vertical = 10 \times 8,\ 10 \times 16,\ 10 \times 32,\ 10 \times 64$). The thickness of the localisation is measured from the inflection points of the profile. (b) Shear band thickness as a function of Q_{mech}/RT. The thickness of the band appears to have an exponential dependency on Q_{mech}/RT.

rectangular mesh with a weak element on one side.

We observe in Fig. 10 that with increasing axial displacement (or time), a pair of conjugate shear bands -in equivalent plastic strain and temperature- are emerging immediately after the material is loaded beyond its yield point. With increasing axial strain, the shear bands are propagating towards the boundaries of the sample, where they eventually reflect around 10% axial strain. It is notable that the localization is progressive, rather than spontaneous, following the timescale of the temperature equation. Also, the thickness of the shear band is evolving with increasing strain. Initially it is determined by the size of the weak element, but with increasing axial strain the shear band's thickness increases to admit the thickness calculated in the previous section.

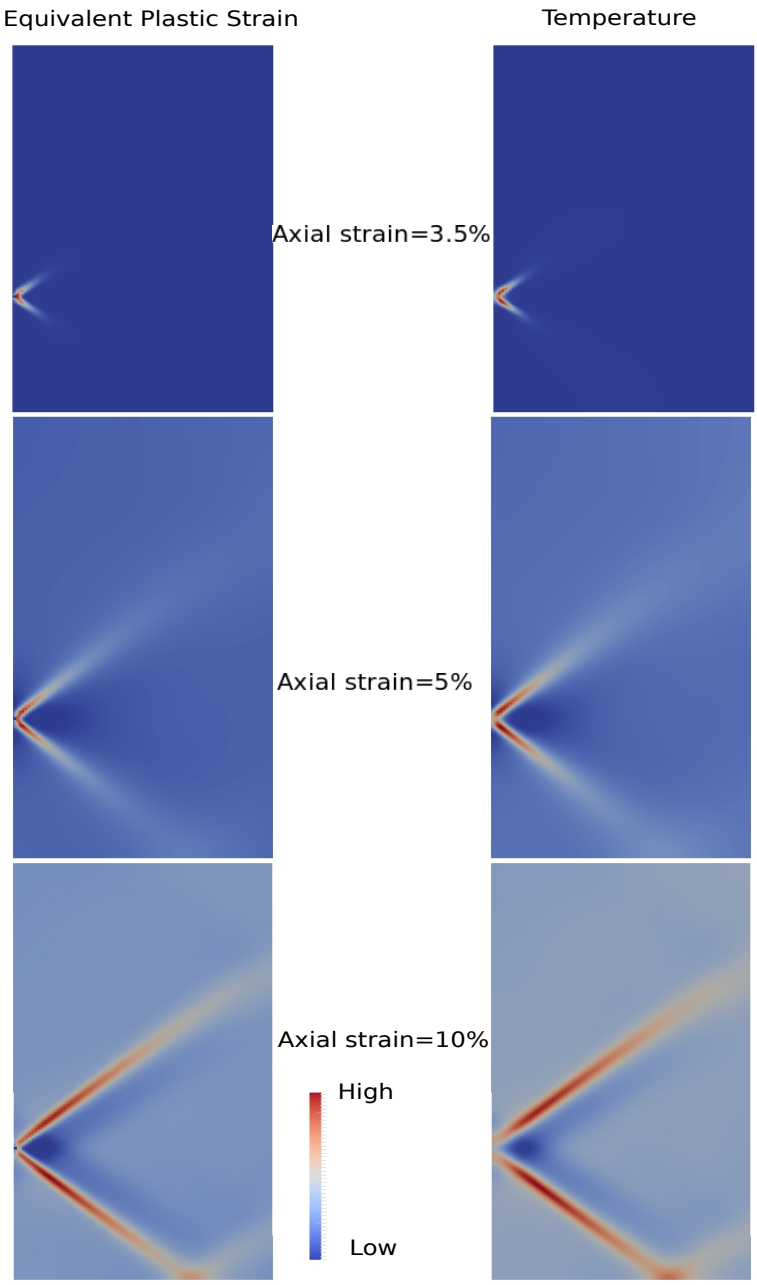

Figure 10: Biaxial loading in a Drucker-Prager elasto-viscoplastic material with thermal sensitivity. The friction coefficient was set to 0.7, normalized cohesion equal to 1, $Ar = 6$, Young's modulus 500 times the cohesion, Poison ratio 0.2, $Gr = 0.335$, $\dot{\epsilon}_0 = 1e5$, $m = 2$ normalized loading velocity 1. Left column is the equivalent plastic strain and right column the temperature profiles, at different axial strains.

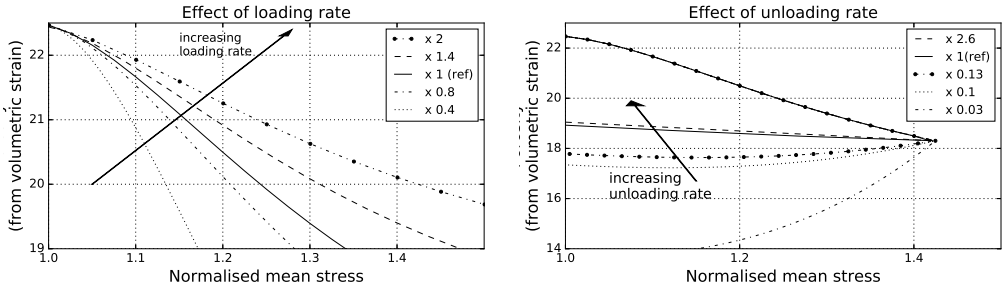

(a) (b)

Figure 11: Effect of loading rate on porosity evolution with respect to normalised mean stress in the compaction regime, under (a) loading and (b) unloading conditions. All comparison are made with respect to a reference case corresponding to the isotropic compression results of dry sandstone from Fortin et al. (2007) (for more details see section 5.1.1 and figure 13).

4.5. Effect of Loading Rate

To demonstrate the rate dependency of the model, two series of isotropic compression simulations were run at different loading and unloading rates and the corresponding evolution of porosity results are shown in Figure (11a,b). In both cases, for loading and unloading, the results are compared with a single reference simulation on sandstone presented in detail in the following sections. For the series of loading simulations, the resulting porosity evolution curves are shown on figure (11a) from the onset of plasticity as the elastic response is rate independent. The results highlight the evolution of the rate of hardening, increasing with the loading rate as expected. Similarly, for the unloading simulations, the results of figure (11b) only show the porosity curves after (and close to) the onset of unloading. Those results highlight the more pronounced creep effect at lower unloading rates.

4.6. Cyclic Loading and Isotropic Hardening

A common limitation of visco-plastic approaches is their difficulty to model cycles of loading and unloading. We test therefore our model on cycles of loading and unloading performed during isotropic compression of rectangular shaped soil specimens of 8 cm high and 4 cm side. The monotonic loading response can be seen in red in figure (12a). When cycles of loading-unloading are performed, however, the creep effects can dominate the response and the model cannot approach the normal consolidation line figure (12a). To alleviate this issue, a mechanism needs to be introduced to account for the re-hardening of the material due to over-consolidation. In consistency plasticity, this is achieved by adjusting the yield surface with an isotropic hardening law. Here, we select instead the equivalent approach of regulating the dissipation of the material when it is over-consolidated. As such, the following formulation is adopted for the activation enthalpy,

$$\Delta Q_{mech} = \alpha (OCR)^{\beta} P'_C \tag{35}$$

where $OCR = \frac{P'_{C,max}}{P'_C}$ is the over-consolidation ratio, $P'_{C,max}$ is the maximum (global) confining pressure that the material has experienced. This power-law model contains two empirical constants, α that controls the hardening of the normally consolidated material and the exponent β that regulates the creep effects in the re-loading phase, as shown in figure (12b).

5. Numerical Analysis of Isotropic and Triaxial Compression Tests

In this section, the theoretical and numerical framework described previously is used to fit a series of laboratory tests for different types of rocks

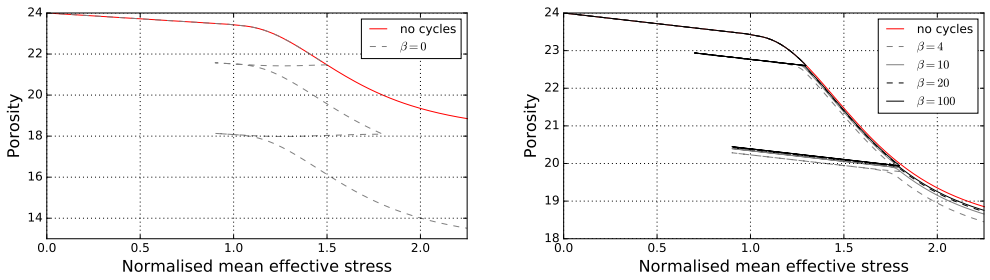

(a) (b)

Figure 12: (a) Figure shows the creep effect in the loading-unloading-reloading cycles if the isotropic hardening doesn't into account for isotropic consolidation. (b) figure showing the loading-unloading (3 cycles) for isotropic consolidation by using OCR.

(sandstone and mudstone), saturating fluids (dry, wet) and stress paths (triaxial, isotropic). Through this fitting exercise we want to constrain the previously unconstrained variable of our visco-plastic flow law, the activation volume V_{act} of Eq. 25. Since this parameter was already discussed to be representing effects like the response of inter-granular interfaces/bonds to the mechanical loading, we expect to obtain critical information on the physics underlining this parameter through the numerical analysis of these tests.

The first sets data to calibrate against concerned the isotropic compression of sandstone and mudstone. This step is performed in order to validate the parameters of the flow law Eq. (16b) from tests in which there is no deviatoric deformation. Thus reducing the complexity of the problem. Once the mechanical parameters of the flow law are constrained, triaxial tests are then fitted to fully constrain the expression of the activation enthalpy presented in equation (16). Following this methodology, the exact form of the activation enthalpy is retrieved. Furthermore, our findings for the two different rocks

are compared and the underlying Physics represented by the aforementioned form of the activation enthalpy is discussed.

5.1. Isotropic Compression Tests

5.1.1. Wet/Dry Sandstone

The isotropic compression tests for sandstone that we are calibrating against are the ones reported by (Fortin et al., 2007). The material used was Bleuswiller sandstone, reporting the variations of porosity and the evolution of elastic wave velocities (shear and compressional wave velocities) for wet and dry situations. Cylindrical sandstone specimens were used of 4cm diameter and 8cm height, with 25% initial porosity, a grain size between 80 and $180\mu m$, and a permeability (in water) of $200 \times 10^{-16} m^2$. The loading tests were conducted at increasing confining pressures up to 280 MPa for both the wet and dry cases, followed by an unloading phase decreasing the confinement back to 0 MPa.

The results of these experiments are shown as dots on figure (13) and show a similar porosity evolution for both the wet and dry scenarios. In both instances indeed, a linear decrease of the porosity with increasing confinement can be observed initially, up to a clearly defined threshold marking the preconsolidation pressure, after which decrease per pressure increment is much larger and no longer linear (during primary and secondary consolidation). The numerical curve was obtained solving the system of equations described earlier for the volumetric part of the flow law:

$$\dot{\epsilon}_v^i = \dot{\epsilon}_0 \left\langle \frac{p' - p'_Y}{\sigma_{ref}} \right\rangle^m \exp\left(-\frac{\Delta Q_{mech}}{RT} \right), \tag{36}$$

Note that the mean stress values presented in this figure are normalised, against the respective preconsolidation pressure value p'_Y for each of the scenarios ($\sigma_{ref} = p'_Y$). Since the experiments were performed under isothermal and drained boundary conditions, temperature variations are negligible, and no excess pore pressure can build up in this quasi-static process so the pore pressure can be ignored altogether. As such, the system degenerates into a classical viscoplastic approach with no feedbacks. As a consequence the pore pressure dependency of the activation enthalpy can be omitted. Furthermore, since under isotropic compression condition there is not deviatoric stress, the activation enthalpy can only be a function of the volumetric work produced per unit area,

$$\Delta Q_{mech} = \Delta E_0 + P_c^{max} \Delta V_{act}^{iso} \tag{37}$$

where P_c^{max} is the maximum pressure that the material experienced (i.e. the OCR). The results of the model for isotropic compression of sandstone can be seen in figure (13).

5.1.2. Isotropic Compression Test for Mudstone

Isotropic compression and triaxial compression test have also been previously performed on Noto diatomaceous mudstone (Oka et al., 2011). In that instance, rectangular-shape specimens were used with 8 cm high and 4 cm side. Similarly to Section 5.1.1, this experiment was simulated numerically and the results, presented in figure (14), show excellent agreement between the simulation and experiments. The porosity evolution follows indeed the exact same pattern as described in section (5.1.1).

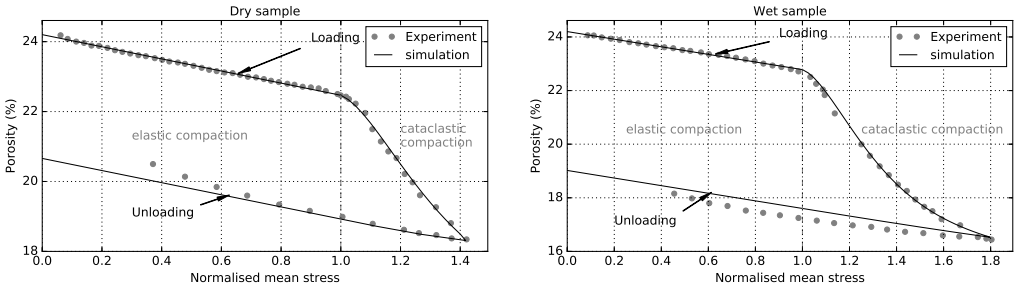

Figure 13: Comparison of numerical and laboratory results for isotropic compression experiments from Fortin et al. (2007) on wet (left) and dry (right) samples. The nice match in both cases is obtained with the same model, with normalization pressures of 132 MPa and 190 MPa respectively for the wet and dry cases. The inverted parameters for the flow law of equation (36) are $\dot{\epsilon}_0 = 10^{-6}\ 1/s$, $m = 3$ and $V_{act}^{iso} = 4.95(J/Pa/mol)$.

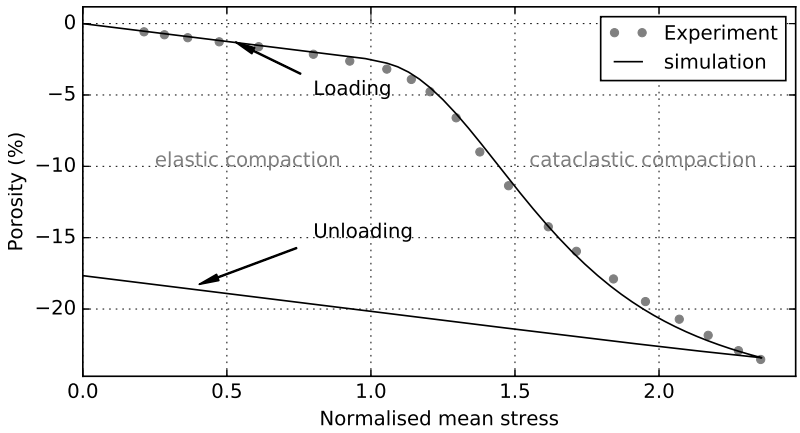

Figure 14: The porosity evolution with increase the effective pressure for mudstone.The inverted parameters for the flow law of equation (36) are $\dot{\epsilon}_0 = 10^{-6}\ 1/s$, $m = 3$ and $V_{act}^{iso} = 5.4(J/Pa/mol)$.

5.2. Triaxial Compression Tests

Triaxial compression experiments represent another important type of tests to validate the model against, especially for sedimentary rocks. Having established the mechanical properties $\dot{\epsilon}_0$, m and V_{act}^{iso} of the visco-plastic flow law of equation (36), this section presents the calibrations of the model against conventional triaxial tests for different types of rocks: sandstone, mudstone. The goal of this section is to use these triaxial experiments where excess pore pressure is generated in the sample, to constrain the form of the activation enthalpy ΔQ_{mech} of the flow law. Recalling the discussion of the introduction and section 3.1, ΔQ_{mech} is expected to have a generic form of the following type for wet experiments:

$$\Delta Q_{mech} = \Delta E_0(q) + P_c^{max} \Delta V_{act}^{iso} + \Delta p_f V_{act} \tag{38}$$

where ΔE_0 is a (stress path dependent) reference value of the activation energy, p_f is the excess pore pressure and V_{act} the activation volume for the pore volume deformation processes. When dry cases are considered, equation (38) is modified to account for density variations instead of the excess pore pressure. Given the above considerations, in this section the values of $\dot{\epsilon}_0$, m and ΔV_{act}^{iso} inverted from the isotropic compression tests are used to invert for E_0 and V_{act} from drained triaxial compression experiments.

5.2.1. Triaxial Compression Test for Sandstone

The first case considered in this section was conducted by (Wong et al., 1997), who conducted a series of triaxial experiments on Adamswiller sandstone under a broad range of effective pressures to identify the transition in

failure mode from brittle faulting to cataclastic flow. Six cylindrical samples were used, cored parallel to the bedding, 38.1 mm long and 18.4 mm in diameter, with 22.6% porosity. The experiments were performed at a fixed loading rate of 5×10^{-5}/s, under confining pressures of 5, 20, 40, 60, 100 and 150 MPa respectively.

Figure (15a) shows the stress paths from the laboratory experiments (Wong et al., 1997) with the corresponding yield points identified by the original authors. See (Wong et al., 1997) for all details regarding the experiments. The data was fit with a cap envelope consisting of a Drucker Prager (Drucker and Prager, 1952) surface in shear and a Modified Cam Clay model as a cap (Roscoe and Burland, 1968), expressed as $\left(\frac{q}{M}\right)^2 + p(p - p_0) = 0$. The preconsolidation stress p_0 and the slope of the critical state line$M$ were inverted from the experimental data and set to $p_0 = 210$ MPa and $M = 1.35$. The Modified Cam Clay was selected as it is more stable numerically than the original Cam Clay formulation.

Those experiments are then modelled numerically following the methodology described previously (see also section 5.2 Poulet and Veveakis (2016)). The experimental curves reported for this sandstone have been fitted by using the material properties listed in table (6) and varying only V_{act} at different confining pressures (see figure 18a) and the formula of ΔQ_{mech} was as shown in equation (38). The results are shown in figures (16a,b) for a constant value of ΔE_0, noticing the derived logarithmic dependence of V_{act} on confining pressure shown in figure (18a):

$$V_{act} = \alpha_0 \left(1 - \frac{\ln P_{c(max)}/P_0}{\ln P_{cs}/P_0}\right) RT = \alpha_0 \frac{RT}{\ln P_{cs}/P_0} \ln \frac{P_{cs}}{P_{c(max)}} \tag{39}$$

In this expression P_{cs} is the effective confining pressure corresponding to

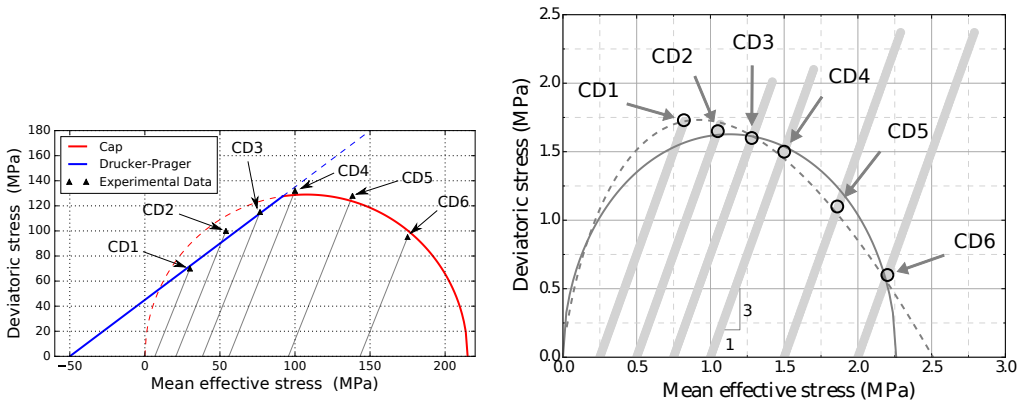

(a) (b)

Figure 15: (a) The experimentally derived yield points (circles) for experiments performed at 6 different confinements (CD 1-6) by (Wong et al., 1997) and the modified cam-clay yield envelope used in modelling the tests (solid line), (b) Best fits of the data using the original Cam Clay (dashed line) and Modified Cam Clay (solid line) models. The experimental stress paths and corresponding yield points were taken from figure 5 in (Oka et al., 2011)

Parameter	Sandstone	Mudstone
$c_{th}\,[\mathrm{m}^2/\mathrm{s}]$	1.3×10^{-6}	1.43×10^{-7}
$k_\pi\,[\mathrm{m}^2]$	1.48×10^{-14}	1.55×10^{-9}
$\mu_f\,[Pa.s]$	8.9×10^{-4}	8.9×10^{-4}
$\beta_m\,[Pa^{-1}]$	2.5×10^{-10}	9.34×10^{-8}
$\dot{\epsilon}_0\,[s^{-1}]$	1.3×10^{-2}	1.36×10^{-3}
$E_{mech}\,[J/mol]$	1000	1345
$\lambda_m\,[K^{-1}]$	3.88×10^{-5}	5.18×10^{-5}
$\sigma'_{ref}\,[MPa]$	189	2.26
$T_{ref}\,[K]$	300	300
$x_{ref}\,[m]$	0.01	0.02
$m\,[-]$	2	2
$\chi\,[-]$	0.65	0.65

Table 6: Parameters used in order to fit the experimental data for sandstone and mudstone. The expression $c_{hy} = k_\pi/\mu_f\beta_m$ have been used for the hydraulic diffusivity where k_π the permeability and μ_f the fluid viscosity.

the critical state for a given stress path. From figure (18a) it can be seen that for the yield envelope used during the inversion (figure 15a), $\alpha_0 = 29.4$. It is to be noted that V_{act} changes sign with confinement, being negative when $P_{cs} < P_{c(max)}$ (i.e. at the "dilatant" shear part of the yield envelope where "brittle" failure is observed in rocks), positive when $P_{cs} > P_{c(max)}$ (i.e. at the "contractant" cap of the yield envelope where "ductile" response is encountered), and zero at critical state $P_{cs} = P_{c(max)}$.

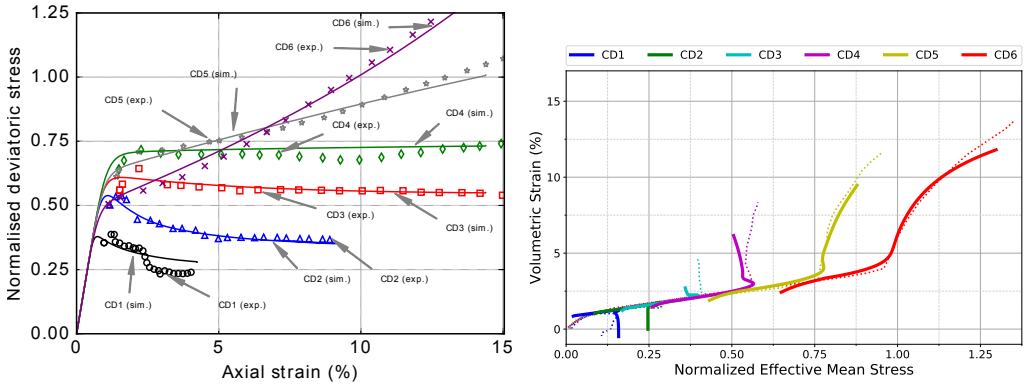

(a) (b)

Figure 16: (a) The deviatoric stress (τ) vs. axial strain results for the experiments (symbols) and the numerical simulations (lines) for sandstone, (b) The volumetric strain versus the effective mean stress results for the experiments (dashed lines) and the numerical simulations (solid lines) for sandstone.

5.2.2. Triaxial Compression Test for Mudstone

The second series of experiments used to validate the model in triaxial compression was performed by (Oka et al., 2011) on diatomaceous mudstone. The test was aiming to demonstrate the existence of compaction bands in this rock and how the variation of the confinement pressure affect on the direction and the inclinations of the strain localization. A series of triaxial tests was performed on six rectangular shaped-prismatic specimens with 8 cm high and 4 cm side. In order to avoid the effect of the initial anisotropy the specimens were taken with their longitudinal direction perpendicular to the plane of sedimentation. Various levels of confining pressure to observe different deformation patterns and the scenarios are listed in table (7). All the tests were conducted up to roughly 20% axial strain.

Following the same methodology described in Section 5.2.1 for sandstone,

Table 7: The selected confinement pressures used in the triaxial test experiment from (Oka et al., 2011)

Case No.	CD1	CD3	CD3	CD4	CD5	CD6
Effective confining pressure (MPa)	0.25	0.5	0.75	1.0	1.5	2.0

a series of numerical experiments are performed using a Modified Cam Clay yield envelope. To match the experimental data, the values of $p_0 = 2.26$ MPa and $M = 1.44$ were selected (see figure (15b). The activation enthalpy ΔQ_{mech} is used as a free parameter which is inverted for in such a way such that its pressure dependency fits the experiment data, as seen in figure (17a,b). The experimental curves reported for this sandstone have been fitted by using the material properties listed in table (6) and varying only V_{act} at different confining pressures (see figure 18b). It can be seen from figure (18b) that in mudstone V_{act} is also following equation (39), with $\alpha_0 = 22.9$.

It needs to be noted that the results are indeed mesh independent. A mesh sensitivity analysis was performed by running multiple simulations with different mesh size scenarios as shown for the stress-strain response of figure 19, for the three-dimensional finite element simulation of the low-confinement CD1 test, which exhibits material softening (Figure 19).

6. Synthesis of the Results

In this work the suggested flow law has been calibrated for triaxial and isotropic experiments in various materials. The dependence of the material's parameters on pressure, temperature and strain rate has been shown to be

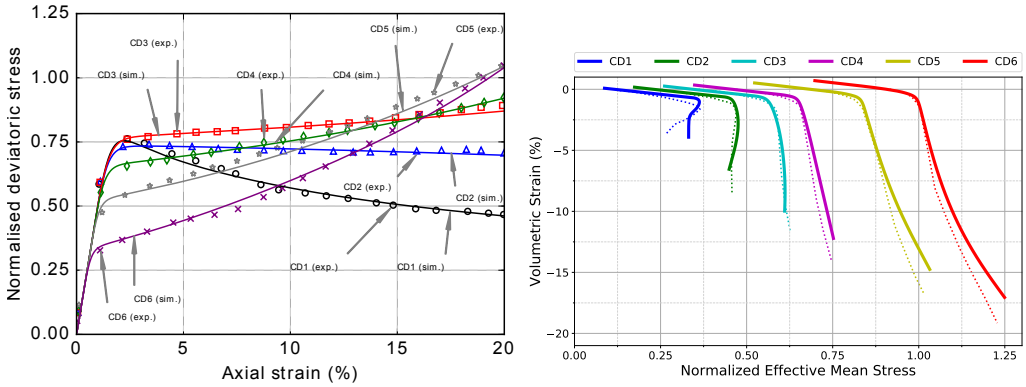

(a) (b)

Figure 17: (a) The deviatoric stress (τ) vs. axial strain results for the experiments (symbols) and the numerical simulations (lines) for mudstone, (b) The volumetric strain versus the effective mean stress results for the experiments (dotted lines) and the numerical simulations (solid lines) for mudstone.

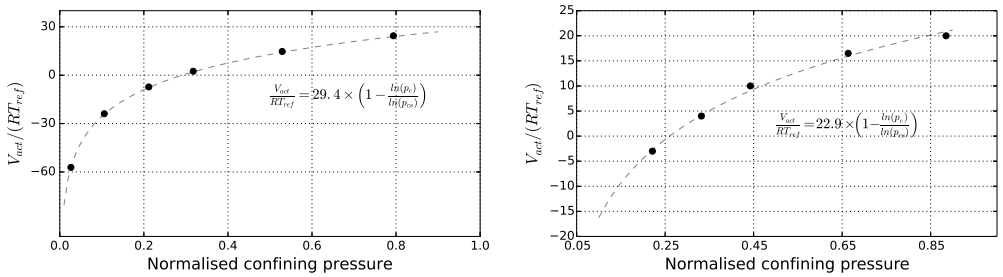

(a) (b)

Figure 18: (a) Dependence of V_{act} with confinement (depth) for sandstone. The condition $V_{act} = 0$ is met at the experiment labelled CD and for lower confinements (CD 1-3) $V_{act} < 0$ and for larger confinements (CD 5-6) $V_{act} > 0$, (b) Dependence of $Vact$ with confinement (depth) for mudstone . The condition $V_{act} = 0$ is met at the experiment labelled between CD 2 and CD 3 and for lower confinements (CD 1 for mudstone) $V_{act} < 0$ and for larger confinements (CD 3-6 for mudstone) $V_{act} > 0$.

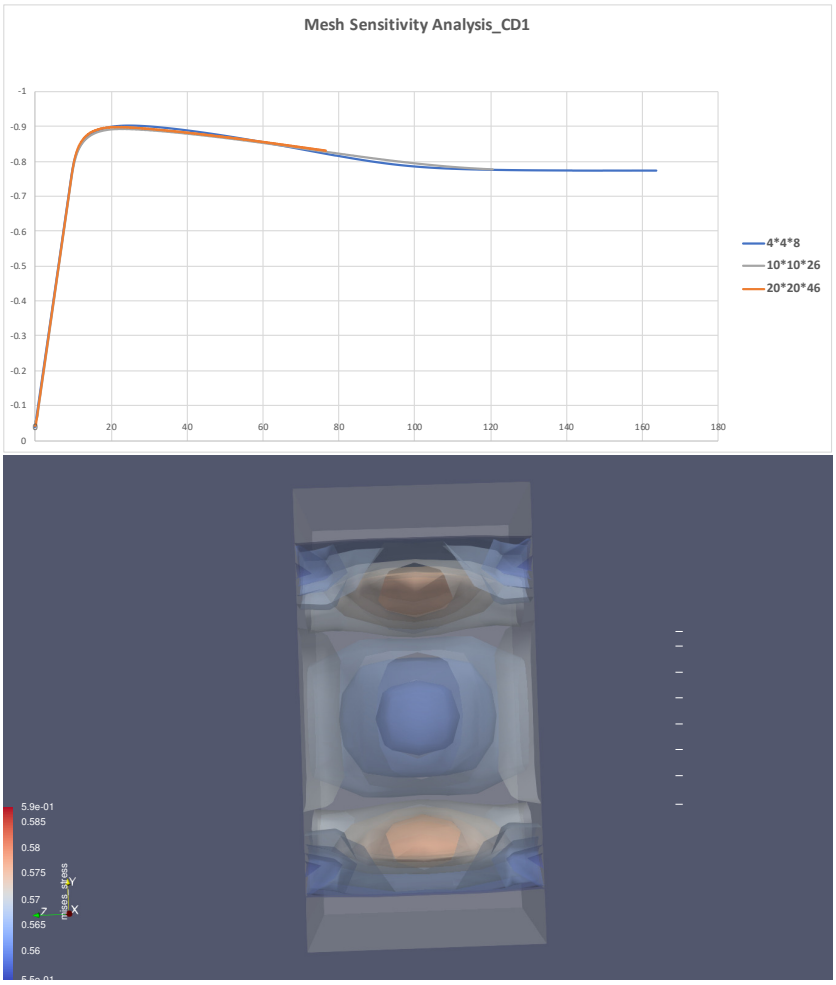

Figure 19: (top) Mesh sensitivity analysis showing the deviatoric stress (τ) vs. axial strain results different simulations of CD1 with different mesh sizes, (bottom)Distribution of Mises stress on a centered vertical slice of models CD1 showing the shear bands

captured adequately by model in its present form, with the power law parameters $\dot{\epsilon}_0$ and m encapsulating the strain rate effects and the activation enthalpy Q_{mech} of the material encompassing thermal and pressure sensitivity:

$$\Delta Q_{mech} = \Delta E_0(P_c^{max}, q) + \Delta p_f V_{act}(P_c^{max}, T) \tag{40}$$

where $\Delta E_0(P_c^{max}, q)$ is a stress path dependent activation energy. It has been shown that ΔQ_{mech} in the present framework acts as a hardening function for the visco-plastic flow law, encompassing physical information of the system on its state variables (temperature and pore pressure). It was therefore shown that accurately determining the mechanisms operating in ΔQ_{mech} and constraining the values of the respective parameters is important for this model to be able to have predictive capability.

6.1. Internal interface mechanisms expressed through the activation volume

From the analysis of all the experimental results, the activation volume V_{act} was shown to obtain a logarithmic dependency with the confining stress (39), that has the form:

$$V_{act} = \alpha_0 \frac{RT}{\ln P_{cs}/P_0} \ln \frac{P_{cs}}{P_{c(max)}} \tag{41}$$

where P_0 is the reference (preconsolidation) pressure, and P_{cs} is a stress path dependent quantity, representing the initial confining pressure corresponding to the critical state for a given stress path. One may immediately observe that this is a relationship akin to Kelvin's equation (F.R.S., 1871) for curved liquid-vapour interfaces,

$$\gamma = \frac{rRT}{2V_m} \ln\left(\frac{p}{p_0}\right), \tag{42}$$

where p and p_0 represent the actual and saturated vapour pressures, r the radius of a droplet, V_{m} the molar volume of the liquid, γ the surface tension, R the universal gas constant and T the temperature. Since Kelvin's law describes the pressure in a liquid-vapor interface, like water bridges in unsaturated samples, the inverted logarithmic law for V_{act} of equation (41) could be seen as expressing the pressure experienced by any grain interface, like solid bridges (cement), water bridges (capillary forces), etc, as discussed in Section 3.2. What remains to be yet evaluated is the physical meaning and processes represented by the fugacity coefficients assumed in the theoretical construction of the model.

6.2. Comparison with the theoretical results of Section 3.2.

Indeed, the considerations of the energetics of the interface processes between the fluid phase and the solid phase in Section 3.2 led to the following expression for V_{act}:

$$V_{act} = \phi_0 \beta_\phi n_c \frac{\rho_f}{\rho_0} \left(\ln \nu_f - \frac{\rho_{sk}}{\rho_f} \ln \nu_{sk}\right) RT \tag{43}$$

Comparing the outcomes of the inversion process (Eq. 41) with the theoretical result of Eq. 43 allows us to equate the two expressions. This procedure provides the following expressions for the coefficient α_0 and the fugacity coefficients ν_{sk}, ν_f:

$$\alpha_0 = P_0 \frac{\rho_f}{\rho_0} \phi_0 \beta_\phi n_c \ln \frac{P_{cs}}{P_0} \tag{44}$$

$$\ln \frac{P_{cs}/P_0}{P_{c(max)}/P_0} = \ln \frac{\nu_f}{\nu_{sk}^{\frac{\rho_{sk}}{\rho_f}}} \Longleftrightarrow \nu_f = \frac{P_{cs}}{P_0} \text{ and } \nu_{sk} = \left[\frac{P_{c(max)}}{P_0}\right]^{\frac{\rho_f}{\rho_{sk}}} \tag{45}$$

For a modified Cam-Clay (mCC) type of yield envelope in triaxial loading, $P_{cs} = \frac{P_0}{2}\left(1 - \frac{M}{\omega}\right)$, where ω is the slope of the stress path ($\omega = 3$ in triaxial loading).

We are therefore deducing that:

1. α_0 is a stress-path pore compressibility quantity, expressing how compressible the porous structure is under a given loading-path. It is maximum ($\alpha_0 \to \infty$) when the material is loaded in isotropic conditions ($\omega \to 0$) and minimum ($\alpha_0 \to -0.69 \frac{P_0 \rho_f \phi_0 \beta_\phi n_c}{\rho_0}$) when the material is loaded in purely deviatoric conditions ($\omega \to \infty$). This intuitive result confirms the experimental observations in sedimentary rocks, suggesting that when materials are loaded in direct shear (i.e. under purely deviatoric conditions) they can deform with minimum pore structure change. This phenomenon (pore structure collapse) is the most pronounced at isotropic compression, as the present approach also concluded.
2. the fugacity coefficient of the fluid phase ν_f is also stress-path dependent and equal to $\frac{P_{cs}}{P_0} = \frac{1}{2}\left(1 - \frac{M}{\omega}\right)$, for a mCC-like material. It determines the effective pressure in the chemical potential of the fluid phase, expressing that the vigorousness of the fluid phase to participate in interface processes depends on the type of mechanical loading

the material undergoes. It can only admit positive values, as it consists the argument of the logarithmic part of the chemical potential, something achieved when $\omega > M$, i.e. when the material is loaded at stress-paths with slopes larger than the critical state line's. This means that skeleton-fluid interface processes are only possible when the deviatoric component of the loading path is preponderant with respect to its isotropic counterpart.

3. the fugacity coefficient of the skeleton ν_{sk} is equal to $\left[\frac{P_{c(max)}}{P_0}\right]^{\frac{\rho_f}{\rho_{sk}}}$, i.e. a power of the maximum pressure the material has experienced $P_{c(max)}$, or equivalently of the minimum Overconsolidation Ratio (OCR) a mCC-type material can admit, $\frac{P_{c(max)}}{P_0}$. The power law is a ratio of the densities, $\frac{\rho_f}{\rho_{sk}}$, becoming linear when the fluid phase has the same density as the solid phase, i.e. at processes like debonding where parts of the solid skeleton get debonded and released in a "fluidized" state.

6.3. Transition from brittle to ductile regime

As it became apparent from the performance of the suggested theory against triaxial data in Section 5.2, the model can transition from a brittle to a ductile response with increasing confinement. The main driver for the model to be able to transition between the two regimes is the change of sign of V_{act}, being negative in the brittle and positive in the ductile regime, as shown in Fig. 18.

By comparing the experimentally derived expression of V_{act}, Eq. (41), we conclude that this change of sign is happening when $P_{cs} = P_{c(max)}$, with $P_{cs} < P_{c(max)}$ being in the brittle regime. This outcome is confirming the experimental observations based on stresses. From the theoretical one of

Eq. (43), we obtain that this change of sign is happening when $\frac{\nu_f}{\frac{\rho_{sk}}{\rho_f}} = 1$, with $\nu_f < \nu_{sk}^{\frac{\rho_{sk}}{\rho_f}}$ being in the brittle regime. This in turns means that, when the partial pressure experienced by the skeleton part of the interface is larger than the partial pressure experienced by the fluid (within a power law exponent $\frac{\rho_{sk}}{\rho_f}$), then the material will follow the predominant solid component and exhibit brittle response. We are therefore able to explain the macroscopic response of rocks based on the microscopic interface process at hand.

7. Conclusions

In conclusion, in this study an elasto-visco-plastic model was suggested based on multiphysical considerations and used to capture the behaviour of sedimentary rocks both in the brittle and ductile regimes. The model was validated against a suite of multi-physics tests in different materials, showing remarkable agreement for a realistic range of material parameters.

Following the performance of the framework against benchmark tests and experimental data, additional conclusions were reached:

1. the dominant mechanism controlling the response of the model in triaxial compression tests is an internal interface mechanism between the skeleton and the pore fluid, akin to the mechanisms expressed through Kelvin's law in water-air capillary interfaces (Eq. 41).
2. the interface process between skeleton and fluid is stress path dependent, being only active when the mechanical loading involves significant deviatoric component. In loadings like isotropic compression, the process is suspended.

3. the introduction of the energy balance equation regularizes the problem of localization of plastic deformation during mechanical softening, providing an internal length and a characteristic time of propagation of the shear band.

The interface model introduced offers some physical intuition about the different mechanisms at play under volumetric and shear-enhanced loading conditions. It allows some quantification of the underlying processes responsible for the different behaviours observed - and intuitively expected - between those two types of deformation. This opens the door to exciting future work to constrain and fully validate the stress-path dependency of the model parameters.

Acknowledgements

This work was supported by resources provided by the Australian Research Council (ARC Discovery grants no. DP170104550, DP170104557), UNSW Sydney and the Pawsey Supercomputing Centre with funding from the Australian Government and the Government of Western Australia. M.V. acknowledges support by the DE-NE0008746- DoE project.

References

Adachi, T., OKA, F., 1982. Constitutive equations for normally conslidated clay based on elasto-viscoplasticity. Soils and FoundationsAND FOUNDATIONS 22 (4), 57–70.

795 Borja, R. I., 1991. Cam-clay plasticity, part ii: Implicit integration of con-
796 stitutive equation based on a nonlinear elastic stress predictor. Computer
797 Methods in Applied Mechanics and Engineering 88 (2), 225–240.

798 Drucker, D. C., Prager, W., 1952. Soil mechanics and plastic analysis or limit
799 design. Quarterly of applied mathematics 10 (2), 157–165.

800 Einav, I., 2012. The unification of hypo-plastic and elasto-plastic theories.
801 International Journal of Solids and Structures 49 (11), 1305 – 1315.
802 URL http://www.sciencedirect.com/science/article/pii/
803 S0020768312000431

804 Eyring, H., 1936. Viscosity, plasticity, and diffusion as examples of absolute
805 reaction rates. The Journal of chemical physics 4 (4), 283–291.

806 Fischer, G. J., Paterson, M. S., 1989. Dilatancy during rock deformation at
807 high temperatures and pressures. Journal of Geophysical Research: Solid
808 Earth 94 (B12), 17607–17617.

809 Fortin, J., Guéguen, Y., Schubnel, A., 2007. Effects of pore collapse and
810 grain crushing on ultrasonic velocities and vp/vs. ournal of Geophysical
811 Research: Solid Earth, B08207.

812 Frost, H., Ashby, M., 1982. Deformation-mechanism maps: the plasticity and
813 creep of metals and ceramics. Pergamon Press.
814 URL https://books.google.com.au/books?id=s9BRAAAAMAAJ

815 F.R.S., S. W. T., 1871. Lx. on the equilibrium of vapour at a curved surface
816 of liquid. The London, Edinburgh, and Dublin Philosophical Magazine and

817 Journal of Science 42 (282), 448–452.
818 URL https://doi.org/10.1080/14786447108640606

819 Gaston, D., Newman, C., Hansen, G., Lebrun-Grandi, D., Oct 2009. Moose:
820 A parallel computational framework for coupled systems of nonlinear equa-
821 tions. Nuclear Engineering and Design 239 (10), 1768–1778.

822 Hill, R., 1963. Elastic properties of reinforced solids: Some theoretical prin-
823 ciples. Journal of the Mechanics and Physics of Solids 11 (5), 357 – 372.

824 Karato, S. (Ed.), 2008. Deformation of Earth Materials. Cambrige University
825 Press.

826 Kauzmann, W., 1941. Flow of solid metals from the standpoint of the
827 chemical-rate theory. Trans. AIME 143, 57–83.

828 Lubliner, J., 1990. Plasticity theory. Macmillan Publishing Company, New
829 York.

830 Muhlhaus, H. B., Vardoulakis, I., 1987. Thickness of shear bands in granular
831 materials. Geotechnique 37 (3), 271–283.

832 Needleman, A., 1988. Material rate dependence and mesh sensitivity in
833 localization problems. Computer Methods in Applied Mechanics and
834 Engineering 67 (1), 69 – 85.
835 URL http://www.sciencedirect.com/science/article/pii/
836 0045782588900692

837 Oka, F., 01 1981. Prediction of time-dependent behaviour of clay. Soil me-

chanics and foundation engineering. Proc. 10th international conference, Stockholm, June 1981. Vol. 1, (A.A.Balkema) 1, 215–218.

Oka, F., 1985. Elasto/viscoplastic constitutive equations with memory and internal variables. Computers and geotechnics 1 (1), 59–69.

Oka, F., Kimoto, S., Higo, Y., Ohta, H., Sanagawa, T., Kodaka, T., 2011. An elasto-viscoplastic model for diatomaceous mudstone and numerical simulation of compaction bands. International Journal for Numerical and Analytical Methods in Geomechanics 35 (2), 244–263.

Orowan, E., jan 1940. Problems of plastic gliding. Proceedings of the Physical Society 52 (1), 8–22.
URL https://doi.org/10.1088%2F0959-5309%2F52%2F1%2F303

Paesold, M., Bassom, A., Regenauer-Lieb, K., Veveakis, M., 2016. Conditions for the localisation of plastic deformation in temperature sensitive viscoplastic materials. Journal of Mechanics of Materials and Structures 11 (2), 113–136.

Perzyna, P., 1966. Fundamental problems in viscoplasticity. Adv. Appl. Mech. 9, 243–377.

Poulet, T., Regenauer-Lieb, K., Karrech, A., Fisher, L., Schaubs, P., 2012. Thermal-hydraulic-mechanical-chemical coupling with damage mechanics using ESCRIPTRT and ABAQUS. Tectonophysics 526-529 (0), 124 – 132.

Poulet, T., Veveakis, M., 2016. A viscoplastic approach for pore collapse in saturated soft rocks using redback: An open-source parallel simulator for

rock mechanics with dissipative feedbacks. Computers and Geotechnics 74, 211 – 221.
URL http://www.sciencedirect.com/science/article/pii/S0266352X15002785

Rashid, M. M., 1993. Incremental kinematics for finite element applications. International Journal for Numerical Methods in Engineering 36 (23), 3937–3956.

Rattez, H., Stefanou, I., Sulem, J., 03 2018a. The importance of thermo-hydro-mechanical couplings and microstructure to strain localization in 3d continua with application to seismic faults. part i: Theory and linear stability analysis. Journal of the Mechanics and Physics of Solids Accepted.

Rattez, H., Stefanou, I., Sulem, J., Veveakis, M., Poulet, T., 2017. Localisation of deformation for shearing of a fault gouge with cosserat microstructure and different couplings. In: Papamichos, E., Papanastasiou, P., Pasternak, E., Dyskin, A. (Eds.), Bifurcation and Degradation of Geomaterials with Engineering Applications. Springer International Publishing, Cham, pp. 155–160.

Rattez, H., Stefanou, I., Sulem, J., Veveakis, M., Poulet, T., 2018b. The importance of thermo-hydro-mechanical couplings and microstructure to strain localization in 3d continua with application to seismic faults. part ii: Numerical implementation and post-bifurcation analysis. Journal of the Mechanics and Physics of Solids 115, 1 – 29.
URL http://www.sciencedirect.com/science/article/pii/S0022509617309638

884 Rice, J. R., 2006. Heating and weakening of faults during earthquake slip. J.
885 Geophys. Res. 111, B05311.

886 Rice, J. R., Lapusta, N., Ranjith, K., 2001. Rate and state dependent friction
887 and the stability of sliding between elastically deformable solids. Journal
888 of the Mechanics and Physics of Solids 49 (9), 1865 – 1898, the {JW}
889 Hutchinson and {JR} Rice 60th Anniversary Issue.

890 Rosakis, P., Rosakis, A., Ravichandran, G., Hodowany, J., 2000. A ther-
891 modynamic internal variable model for the partition of plastic work into
892 heat and stored energy in metals. Journal of the Mechanics and Physics
893 of Solids 48 (3), 581 – 607.
894 URL http://www.sciencedirect.com/science/article/pii/
895 S0022509699000484

896 Roscoe, K., Burland, J., 01 1968. On the generalized stress-strain behavior
897 of wet clays. Cambridge University Press.

898 Rudnicki, J., Rice, J., 1975. Conditions for the localization of deformation in
899 pressure sensitive dilatant materials. J. Mech. Phys. Solids 23, 371–394.

900 Sluys, L., 01 1992. Wave propagation, localisation and dispersion in softening
901 solids. Ph.D. thesis, Technische University.

902 Sulem, J., Stefanou, I., Veveakis, M., 06 2011. Stability analysis of undrained
903 adiabatic shearing of a rock layer with cosserat microstructure. Granular
904 Matter 13, 261–268.

905 Taylor, G., Quinney, H., 1934a. The latent energy remaining in a metal after
906 cold working. Proc. R. Soc., Ser. A. 143, 307 – 326.

907 Taylor, G., Quinney, H., 1934b. The latent energy remaining in a metal after
908 cold working. Proc. R. Soc., Ser. A. 143, 307 – 326.

909 Terzaghi, K., 1925. Erdbaumechanik auf bodenphysikalischer grundlage.
910 Leipzig ; Wien : F. Deuticke.

911 Vardoulakis, I., Sulem, J. (Eds.), 1995. Bifurcation Analysis in Geomechan-
912 ics. Blankie Acc. and Professional.

913 Veveakis, E., Regenauer-Lieb, 2015. Cnoidal waves in solids. Journal of Me-
914 chanics and Physics of Solids 78, 231–248.

915 Veveakis, E., Stefanou, I., Sulem, J., 2013. Failure in shear bands for granu-
916 lar materials: thermo-hydro-chemo-mechanical effects. Geotechnique Let.
917 3 (2), 31–36.

918 Veveakis, E., Sulem, J., Stefanou, I., 2012. Modeling of fault gouges with
919 cosserat continuum mechanics: Influence of thermal pressurization and
920 chemical decomposition as coseismic weakening mechanisms. Journal of
921 Structural Geology 38, 254 – 264, physico-Chemical Processes in Seismic
922 Faults.
923 URL http://www.sciencedirect.com/science/article/pii/
924 S0191814111001623

925 Wang, W. M., Sluys, L. J., de Borst, R., 1997. Viscoplasticity for instabilities
926 due to strain softening and strain-rate softening. International Journal for
927 Numerical Methods in Engineering 40 (20), 3839–3864.
928 URL http://dx.doi.org/10.1002/(SICI)1097-0207(19971030)40:
929 20<3839::AID-NME245>3.0.CO;2-6

930 Wong, T., David, C., Zhu, W., 1997. The transition from brittle faulting to
931 cataclastic flow in porous sandstones: Mechanical deformation. Journal of
932 Geophysical Research: Solid Earth 102 (B2), 3009–3025.

933 Zhang, Y., Buscarnera, G., 02 2017. A rate-dependent breakage model based
934 on the kinetics of crack growth at the grain scale. Ge?otechnique.